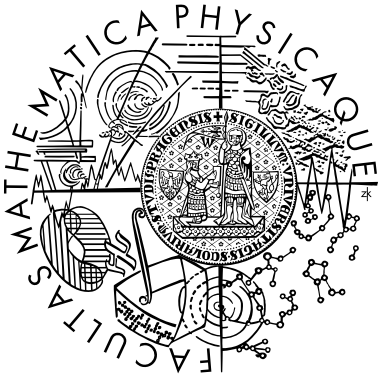

FACULTY
OF MATHEMATICS
AND PHYSICS
Charles University

MASTER THESIS

Lukáš Ohnoutek

Physics of interfaces in magnetic nano structures

Institute of Physics of Charles University

Supervisor of the master thesis:	RNDr. Martin Veis, PhD.
Study programme:	Physics
Study branch:	Optics and Optoelectronics

Prague 2017

I declare that I carried out this master thesis independently, and only with the cited sources, literature and other professional sources.

I understand that my work relates to the rights and obligations under the Act No. 121/2000 Sb., the Copyright Act, as amended, in particular the fact that the Charles University has the right to conclude a license agreement on the use of this work as a school work pursuant to Section 60 subsection 1 of the Copyright Act.

In ..... date ..... signature of the author

Title: Physics of interfaces in magnetic nano structures

Author: Lukáš Ohnoutek

Institute: Institute of Physics of Charles University

Supervisor: RNDr. Martin Veis, PhD., Institute of Physics of Charles University

Abstract: Modification of interfaces in nanostructures can significantly influence their overall properties. Magneto-optical spectroscopy and spectroscopic ellipsometry are ideal for studying these phenomena thanks to their in-depth sensitivity and contactless measurements. Two methods of nonreversible modification of magnetic properties, especially the magnetic anisotropy, are investigated. The measured spectral dependence of magneto-optical Kerr effect is compared to a theoretical calculation in order to determine the profile of the samples for different levels and methods of modification. In addition to this, ellipsometric measurements are performed on a device whose optical properties change by voltage application.

Keywords: interfaces, magnetic anisotropy, magneto-optical Kerr effect, magneto-optical spectroscopy, spectroscopic ellipsometry

I would like to thank my supervisor Dr. Veis for his guidance and the opportunities he has given me to improve my skills and to work on up-to-date research. I really appreciated his friendly approach and the good atmosphere in the laboratory.

I also thank my consultant Lukáš Beran. The discussions with him were always fruitful and often helped me when I was stuck on a problem.

A special thanks goes to my family and Michael for their love and endless support.

I acknowledge the support of Charles University, project GA UK No. 1578217 to the research presented in this thesis.

Contents

Introduction

The discovery of giant magnetoresistance in 1988 laid the foundations of a new field of physics - spintronics. Spintronics aims to create devices that will use not only the electron's charge but also its spin in data processing, transport and storage. Due to the connection between the spin of the electron and magnetization, magnetic materials are naturally essential in spintronic devices.

These materials already play a significant role in current data storage technology. Compared to another device storing digital information - the random access memory (RAM) - magnetic memories are non-volatile which means that the information is retained even when the power is off. The most wide-spread magnetic memory is the hard disk drive (HDD) allowing the storage of large volumes of information for a low price. However, HDDs have slow data access times and high energy consumption [1]. That is why new designs of magnetic memories have been suggested, hopefully leading to a memory device combining the non-volatility of HDDs and fast access times of RAMs. Magnetic random access memory (MRAM) is already commercially available [1]. It offers about 10000 times faster data access than HDDs [2]. More products have been proposed and are currently under development such as the racetrack memory [3].

As mentioned above, spintronics not only aims to use the electron's spin for storing information but it also aspires to utilize it in data processing. Alternative ways of processing data are gaining more importance now that the current ways by which the computers have been getting more powerful are nearing its limits [4]. For example, magnetic domain-wall logic [5] promises lower-powered and higher-speed devices than the current technologies [2].

For all of the spintronic devices, it is important to prepare magnetic layers with desired properties. Atoms on the surface of a layer or on an interface with another layer have different boundary conditions than the atoms in bulk and hence they also exhibit different properties. In thin films, these atoms make up a greater percentage of the volume of the material. Therefore changes at the interfaces can influence the overall properties of a nanostructure. For the research in this area, it is important to understand the origin of the modification of the magnetic properties.

However, modifications of interfaces affect not only magnetic properties but a number of other material's characteristics which allows controlling these properties by tailoring the interfaces.

Two methods of irreversible modifications of magnetic properties are investigated in this work. The first one is by irradiation with Ga^+ ions and the second one by a single pulse of soft X-rays. Both of these techniques also allow patterning of magnetic properties. Samples of different compositions are studied by magneto-optical spectroscopy and the profiles of the samples are determined by the comparison between the experiment and theoretical calculations based on 4×4 matrix formalism for anisotropic media.

In addition to this, a way of changing the optical properties of nanostructures through modifying interfaces is demonstrated in this work.

This work is divided into 6 chapters.

In the first chapter, the changes of magnetic properties are discussed with an

emphasis on magnetic anisotropy. At first, the different contributions towards magnetic anisotropy of thin films are mentioned. Then the magnetic anisotropy of sandwiches with Co layers is discussed. Finally, various methods of modifying the anisotropy are presented and the current state of research into some of the methods is summarized.

As the experimental methods used in this work utilize polarized light it is important to show how to describe it which is done in chapter 2. Magneto-optical parameters are also introduced in this chapter.

In the third chapter, the 4×4 transfer matrix formalism for anisotropic media which allows the theoretical calculations of magneto-optical response is described.

The next chapter presents the experimental methods used in this thesis.

The studied samples and the methods of their preparation and modification are laid out in chapter 5.

In the last chapter, the achieved results are presented. This chapter is followed by conclusions which summarize the results.

1. Magnetic properties and their modification

Magnetic materials can have their magnetic moments ordered in various ways. Based on this magnetic ordering materials can be divided into diamagnets, paramagnets, ferromagnets, ferrimagnets and antiferromagnets. Each of these classes of materials has a characteristic hysteresis loop, i.e. the dependence of the material's magnetization on the external magnetic field. This work concentrates on ferromagnetic materials. The magnetic properties whose modifications are discussed can be determined from the hysteresis loop of the studied material. These properties are namely: saturation magnetization, coercive field, magnetization in zero external field and magnetic anisotropy. Special attention is paid to the changes of magnetic anisotropy due to the possible application of the process in preparation of nanostructures with perpendicular magnetic anisotropy (PMA) or patterning of magnetic properties in the industry.

In the first part of this chapter magnetic anisotropy is discussed, at first in general, and then specifically for nanostructures with thin layers of cobalt. In the rest of the chapter, a few methods of the modification of magnetic properties are presented. These can be reversible or non-reversible. The techniques studied in this work are debated in greater detail.

1.1 Magnetic anisotropy of thin films

Ferromagnetic materials usually have one or more easy axes along which the magnetization in domains tends to lie. The leading term of the anisotropy energy E_a can be expressed as [6]

$$E_a = K_a \sin^2 \theta, \tag{1.1}$$

where K_a is the anisotropy constant and θ is the angle between the direction of the magnetization and the easy axis.

The overall magnetic anisotropy of the system is influenced by the shape of the sample, magneto-crystalline anisotropy, strain and the surface anisotropy.

Shape anisotropy is connected to the demagnetizing field in the sample which depends on the shape. In the special case of a ferromagnetic ellipsoid the magnetostatic energy is given by [6]

$$\varepsilon_m = \frac{1}{2}\mu_0 V \mathcal{N} M_s^2, \tag{1.2}$$

where μ_0 is the permeability constant, V is the volume of the ellipsoid, $\mathcal{N}$ is the demagnetizing factor and M_s is the magnetization.

The demagnetizing factor $\mathcal{N}$ differs for the cases when the ellipsoid is magnetized along the easy axis and along the hard axis. Therefore also the magnetostatic energy varies between these two cases. The difference between these energies is related to the anisotropy energy.

The shape anisotropy constant can be written as [6]

$$K_{sh} = \frac{1}{4}\mu_0 M_s^2 (1 - 3\mathcal{N}'), \tag{1.3}$$

where the $\mathcal{N}'$ stands for the demagnitizing factor in the easy direction.

The shape anisotropy is strong only for small samples. In the case of thin films, the shape anisotropy is substantial and results in an in-plane anisotropy unless other contributions are stronger.

Magneto-crystalline anisotropy expresses in the way that certain directions in the crystal lattice are preferable for the magnetization to point in. One of the origins of this anisotropy is the electrostatic interaction of the orbitals which contain magnetic electrons with the field created by the rest of the crystal (single-ion contributions) [6]. The anisotropy of the dipole-dipole interaction (it is energetically favorable for dipoles to align head-to-tail rather than broadside) together with the anisotropic exchange give rise to the two-ion contributions [6].

Because of the magneto-crystalline anisotropy, the unique easy axis of cobalt crystallized in a hexagonal close packed lattice is the hexagonal axis [6].

Uniaxial anisotropy in a ferromagnet can also be induced by uniaxial stress σ. Again, this effect can be explained by single-ion and double-ion contributions. The stress-induced anisotropy constant has the form [6]

$$K_{a\sigma} = \frac{3}{2}\sigma\lambda_s. \tag{1.4}$$

λ_s is the saturation magnetostriction.

For thin films, there is an additional contribution to the overall anisotropy of the structure - the surface (or interface) anisotropy.

The single-ion mechanism plays a significant role in the surface anisotropy [6]. The orbitals with magnetic electrons interact with the crystal field. However, in the case of atoms on the surface, the crystal field is influenced by the anisotropic surroundings of the atoms so the magnetic moments tend to align in a different way than the moments in the bulk.

Also, for epitaxial structures strain can be induced by the lattice mismatch between the epitaxial layer and the substrate which can result in a stress-induced anisotropy.

The contribution of the surface anisotropy towards the overall effective anisotropy scales with the thickness of the film t. The effective anisotropy constant K_{eff} can be written as [6]

$$K_{eff} = K_v + \frac{K_s}{t}, \tag{1.5}$$

where K_v denotes the volume and K_s the surface contribution.

1.2 Magnetic anisotropy of cobalt nanostructures

Magnetic anisotropy of ultrathin cobalt multilayers depends on the thickness of the cobalt layer [7]. Cobalt films thinner than the spin-reorientation transition thickness d_{SRT} exhibit PMA and thicker films have in-plane anisotropy.

As explained in section 1.1, the effective magnetic anisotropy arises from the interplay of different contributions.

Bertero et al sputter deposited Pt/Co multilayers under different conditions (sputtering pressure and gas, substrate temperature) in order to study the effect

of the conditions on the magnetic properties, especially PMA [8]. The cobalt layers were ultrathin (≤ 6 Å) therefore the contribution of the surface anisotropy towards the effective anisotropy was high. The films sputtered in Xe showed a better quality of layering, i.e. sharper interfaces, than the ones sputtered in Ar. At the same time, the Xe sputtered films had a higher PMA. This result indicates that the intermixing of Co and Pt at the interfaces strongly influences the resulting magnetic anisotropy of the nanostructures.

This hypothesis is further supported by more experiments including the X-ray magnetic circular dichroism measurements on films sputtered in different gases [9]. The difference in the amount of intermixing of Pt and Co when the layers are sputtered in Ar and Xe can be attributed to a bombardment of the growing film by Ar backscattered neutrals [10]. PMA is strongest for sharp interfaces and it degrades with intermixing [9]. Bertero et al explain this based on the Néel-like anisotropy model [11]. Spin-spin exchange coupling, spin-orbit coupling and orbit-crystal-field coupling all have to be present for structural anisotropy to result in magnetic anisotropy. Spin-spin interaction is demonstrated by the ferromagnetism of cobalt. Spin population together with uncompensated orbital moments then result in magnetic anisotropy. When the interface is sharp there is a large spin-polarized population at the interface thanks to Co moments. Pt near the interface is also spin polarized by the neighboring Co atoms [12]. There are also a lot of uncompensated orbital moments on the interface because of it being sharp. In the case of intermixing the polarization of Pt reaches further because of the Co being diluted in Pt. However, in this case, the orbital moments are partially compensated hence the resulting magnetic anisotropy is smaller.

Because Pt and Co have different lattice constants strain is induced both in Pt and Co when they are grown on top of each other. There is a correlation between the lattice strain and the observed magnetic anisotropy [13]. The volume contribution towards the overall anisotropy constant can be generally written as [13]

$$K_v = -\frac{1}{2}\mu_0 M_s^2 + K - \text{constant}\lambda_s\sigma, \tag{1.6}$$

where K represents the magneto-crystalline anisotropy.

If $(\lambda_s\sigma)$ is negative the easy axis lies in the plane perpendicular to the stress axis [13]. For hexagonal close packed cobalt $\lambda_s < 0$ [14]. Therefore there will be a contribution towards PMA if the stress is applied in the in-plane direction and the Co layer is under tension ($\sigma > 0$) which is the case of Co grown on Pt. Zhang et al conclude that even though there are other contributions to anisotropy such as the mixing at the interfaces mentioned above strain has to be taken into account when studying the anisotropy of thin cobalt films [13].

It has been shown that the non-magnetic overlayer of the cobalt film has an effect on the magnetic anisotropy of the nanostructure as well [15, 16]. This behavior can be attributed to hybridization of the orbitals of atoms at the interface [16]. The anisotropy depends both on the material of the overlayer and the thickness of the overlayer [16].

1.3 Methods of modification of magnetic properties

As described above the surface magnetic anisotropy can significantly influence the total anisotropy of nanostructures. The methods which are discussed in the following text modify the interfaces in nanostructures which results in the change of the magnetic anisotropy.

1.3.1 Irradiation by Ga^+ ions

Irradiation by energetic ions can be used for patterning of magnetic properties [17]. Collisional intermixing at the interfaces is induced by the bombarding ions [18].

Maziewski et al [19] studied the effects the irradiation by different Ga^+ ion fluences has on Pt/Co/Pt structures depending on the ion fluence and the thickness of the Co layer. A 20 nm Mo buffer layer, a 20 nm Pt layer, a wedge-like Co layer (d_{Co} thickness between 0 and 5 nm) and a 5 nm Pt cover layer were deposited by molecular beam epitaxy (MBE) on an Al_2O_3 substrate in order to do this. The spin-reorientation transition occurred at $d_{SRT} = 2.2$ nm. This sample was subsequently irradiated by 30 keV Ga^+ ions with the ion fluence varying in the direction perpendicular to the gradient of the Co layer thickness. The mean in-depth implantation was 10 nm for this energy.

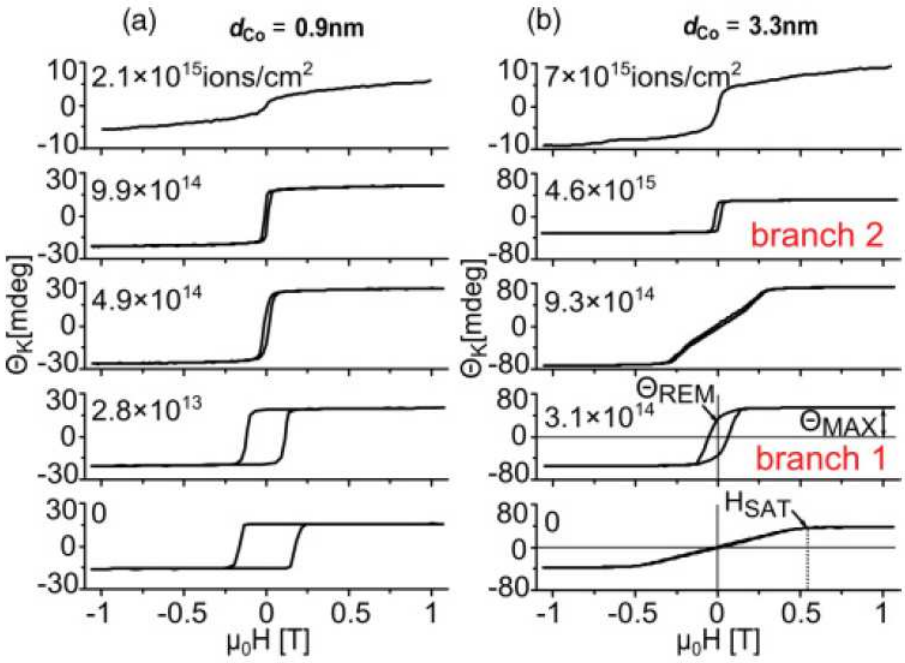

Figure 1.1: Polar magneto-optical Kerr rotation θ_K hysteresis loops measured by Maziewski et al for the Co film 0.9 nm and 3.3 nm thick after irradiation with various ion fluences. H represents the magnetic field intensity, H_{sat} is the saturation field, θ_{max} the maximum Kerr rotation and θ_{rem} the remanent Kerr rotation. The picture is taken from Ref. [19].

Polar magneto-optical Kerr rotation (PMOKR) hysteresis loops were mea-

sured at different places of the sample (corresponding to a certain Co layer thickness and irradiation with a specific ion fluence).

PMOKR loops for two different thicknesses of the Co layer, one below the d_{SRT} thickness and one above, after irradiation with various ion fluences are shown in figure 1.1. The PMOKR is directly proportional to the out-of-plane component of a material's magnetization vector. The hysteresis loops in figure 1.1 therefore give an information about the magnetic anisotropy for a specific Co layer thickness and ion fluence. For $d_{Co} = 0.9$ nm the magnetic anisotropy is originally out-of-plane because the out-of-plane component of magnetization is non-zero for a zero outer magnetic field. With irradiation, the coercive field H_c reduces until the sample exhibits superparamagnetic behavior.

Superparamagnetism applies to ferromagnetic particles for which the product of the anisotropy constant K_a and their volume V is less than or similar to the thermal energy k_BT. This results in the sum of the magnetic moments in the particle fluctuating randomly [6].

For the thickness $d_{Co} = 3.3$ nm the magnetic anisotropy is originally in-plane (the out-of-plane axis of the film is a hard axis). Irradiation with certain ion fluences changes the anisotropy to out-of-plane.

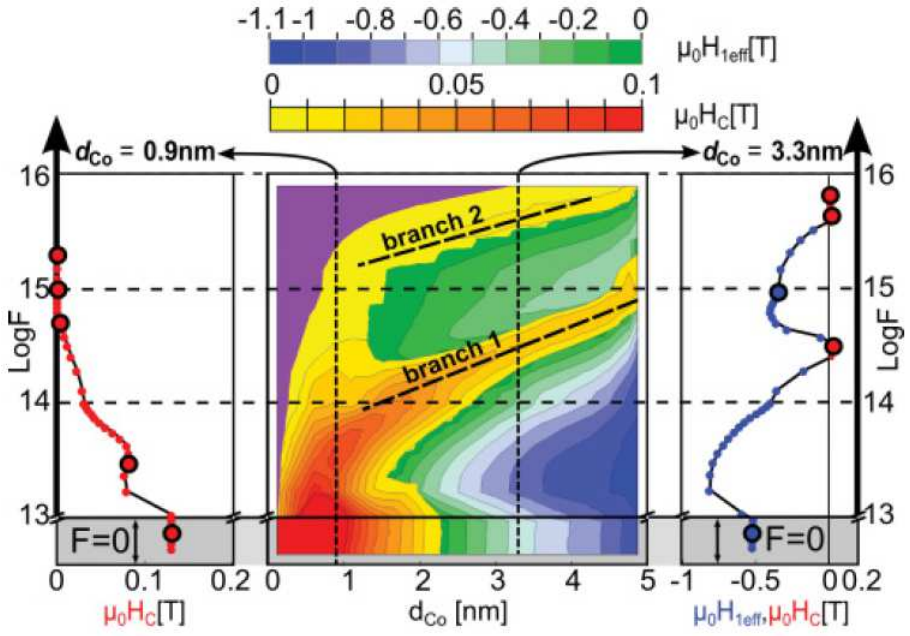

Figure 1.2: A colour map showing the dependence of H_c or H_{1eff} on the Co film thickness d_{Co} and the ion fluence F for the Pt/Co/Pt multilayer. The picture is taken from Ref. [19].

As illustrated in figure 1.1 the coercive field H_c for a PMA state and the saturation field H_{sat} for an in-plane anisotropy state can be determined from the hysteresis loops. In case of a film for which the preferred magnetization direction is in-plane, H_{sat} represents the effective anisotropy field H_{1eff}. The parameters H_c (for a state with PMA) and H_{1eff} (for a state with in-plane anisotropy) are plotted as a function of the Co film thickness and the ion fluence in the form of a color map shown in figure 1.2. Two "branches" of induced PMA are visible on this map.

Maziewski et al [19] explain the observed changes in magnetic anisotropy upon irradiation by two mechanisms - the intermixing at the interfaces and the formation of ordered CoPt alloys. As discussed in section 1.2, intermixing of Pt and Co atoms reduces the PMA. On the other hand, some CoPt alloys exhibit higher anisotropy than pure Co films [20]. Therefore these mechanisms compete and the effect of ion irradiation depends on which mechanism is dominant.

The formation of the ordered $L1_0$ CoPt alloy is evidenced by a number of experiments [19] performed by Maziewski et al. The lattice parameter deduced from the high-resolution transmission electron microscopy (HRTEM) images taken on a sample with $d_{Co} = 3.3$ nm irradiated by $F = 2.8 \times 10^{14}$ ions/cm^2 (from branch 1) matches the lattice parameter of the $L1_0$ alloy. The energy dispersive X-ray analysis (EDXA) carried out on the same sample gives a similar chemical composition to the $L1_0$ alloy in the depth of the Co layer.

Furthermore, the Co K-edge X-ray magnetic circular dichroism (XMCD) was measured on a non-irradiated sample with $d_{Co} = 3.3$ nm, an irradiated sample (same d_{Co}, $F = 2.8 \times 10^{14}$ ions/cm^2) and a reference ordered $L1_0$ CoPt alloy. The XMCD spectrum of the irradiated sample can be interpreted as a sum of contributions from pure Co and $L1_0$ alloy.

Sakamaki et al performed Co K-edge extended X-ray absorption fine structure (EXAFS) measurements on Al_2O_3/Pt (4.5 nm)/Co (2.4 nm)/Pt (3.5 nm) nanostructures prepared by sputter deposition [21]. These measurements reveal that the in-plane lattice constant of Co is expanded by 4.8 % upon irradiation with $F = 1.5 \times 10^{14}$ Ga^+ ions/cm^2 while the out-of-plane one is only expanded by 2.4 %. Such a difference in the lattice constant for different directions should enhance PMA. For a higher ion fluence $F = 4 \times 10^{14}$ ions/cm^2, both the in-plane and the out-of-plane lattice constants expand by a similar percentage. The crystal structure is isotropic in this case and the PMA should disappear. Therefore, anisotropic strains caused by ion irradiation should also be considered when trying to explain the observed effects. EXAFS measurements also confirm the Co-Pt intermixing [21].

The work in Ref. [19] was extended by Mazalski et al [22]. In their work both Ga^+ and He^+ ions were used to irradiate samples with the same composition as the ones in Ref. [19]. Different kinds of irradiating ions result in different modifications of magnetic properties [23]. The energy of the ions was 30 keV which meant that the penetration depth of the He^+ ions was 400 nm.

When a map similar to the one shown in figure 1.2 is plotted two branches of enhanced magnetic anisotropy are visible for both of the irradiating ion types (not shown). However, only Ga^+ ions induce PMA. This can be attributed to the difference in the mass of the ions. Heavy ions cause ballistic mixing while light ions create dilute vacancy-interstitial pairs which are highly mobile and hence a return to the thermodynamically stable state often occurs [24].

Monte Carlo and classical molecular dynamics simulations of irradiating the Pt/Co/Pt structures by 30 keV Ga^+ ions confirm the creation of ordered CoPt alloys [25]. However, the authors did not find a correlation between the ordered alloy creation and the observed magnetic anisotropy. Also, the volume of the ordered alloys created after ion irradiation is small according to the simulations. The simulations predict an induction of strain. The authors suggest that the induced strain is at the origin of the observed changes of magnetic properties.

Au/Co nanostructures exhibit PMA [26]. Au, unlike Pt, is immiscible with Co [27]. Therefore, the ion induced intermixing at the Au/Co interface differs from the intermixing at the Pt/Co interface. Mazalski et al grew a 20 nm Pt underlayer, a Co wedge (d_{Co} = 0-5 nm) and a 5 nm Au overlayer by MBE on an Al_2O_3 substrate [27]. This sample was then irradiated by 30 keV Ga^+ ions. The fluence of the ions varied in the direction perpendicular to the gradient of the thickness of the Co layer. Tridyn simulations of atomic collisions [28] show that the ions penetrate both of the interfaces of the Co layer [27].

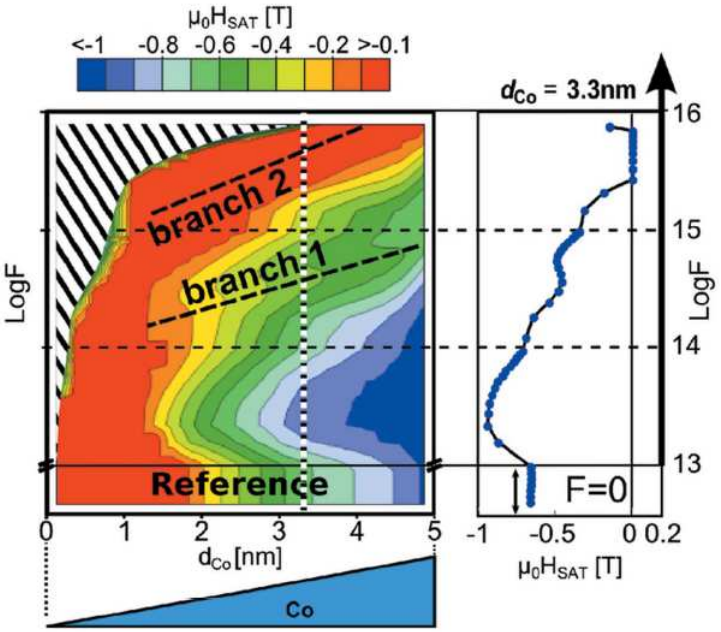

Figure 1.3: A colour map showing the dependence of H_{sat} on the Co film thickness d_{Co} and the ion fluence F for the Pt/Co/Au multilayer. Areas represented by red colour correspond to areas with PMA. The picture is taken from Ref. [27].

The same way as described above a color map was made based on the saturation field H_{sat} determined from PMOKR hysteresis loops measured at different places of the sample. The colour map is shown in figure 1.3. Areas represented by red color correspond to areas with PMA. Compared to the map in figure 1.2 the first branch has an increased saturation field but does not exhibit PMA. PMA is still present for the second branch. The top Co interface seems to contribute to the changes of magnetic properties upon irradiation more than the lower interface.

The Co K-edge XMCD spectra measured on a sample with d_{Co} = 3.3 nm and Au capping layer after irradiation with fluences corresponding to branch 1 and 2 resemble the spectrum of the ordered $L1_0$ alloy. Mixing of Au and Co does not modify the XMCD spectrum. Mazalski et al conclude that the observed changes of magnetic properties appear due to intermixing and formation of ordered Co-Pt alloys at the bottom Co interface.

The spectral dependence of polar magneto-optical Kerr effect (PMOKE) of Co_xPt_{1-x} alloys varies with x [29]. This can be used to determine the level of intermixing at the Co/Pt interfaces from measuring PMOKE spectra. Jakubisová-Lišková et al measured PMOKE spectra of Pt/Co/Pt non-irradiated samples and samples irradiated with a few fluences of 30 keV Ga^+ ions [30, 31]. The mea-

sured PMOKE spectra were compared with optical multilayer models and the profile of the samples was determined from the best fit between the model and the experiment. The same approach is used in this work.

1.3.2 Irradiation by intensive laser pulses

Thermal treatment of Pt/Co and Au/Co nanostructures affects their magnetic properties. Due to the different miscibility of Pt and Au with Co mentioned in section 1.3.1 the effect of annealing is opposite for Pt/Co and Au/Co bilayers. Thermal treatment of Pt/Co nanostructures leads to intermixing at the interface [32] which results in a decrease of magnetic anisotropy [9]. In the case of Au/Co multilayers, the interfaces are sharpened by annealing which leads to the creation of PMA (for thin enough layers) [33].

The temperature in metals can be locally increased by light absorption. Therefore intensive laser pulses can locally anneal nanostructures and cause local irreversible changes of magnetic properties. This is a promising method of magnetic patterning as interference lithography can be used [34]. An irreversible decrease of magnetic anisotropy induced by light irradiation has been reported in Pt/Co multilayers [35, 36]. For a thin Co film sandwiched with Au layers irradiation with laser pulses leads to an irreversible increase of the magnetic anisotropy [37].

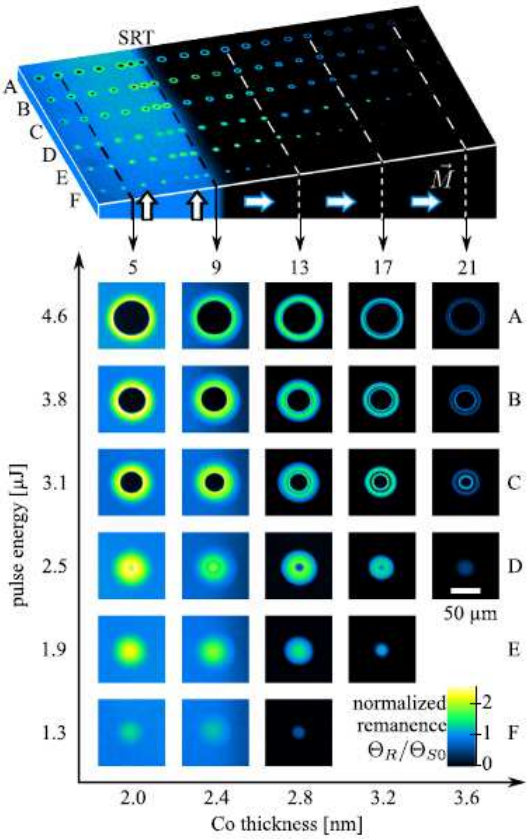

Figure 1.4: A PMOKE normalized remanence image of Pt/Co/Pt after irradiation with single laser pulses of wavelength 800 nm. θ_{SO} is the maximum of Kerr rotation in the region before irradiation. The picture is taken from Ref. [38].

Kisielewski et al subjected Pt (5 nm)/Co wedge (d_{Co} =1.5-5 nm)/Pt (5 nm)

multilayers grown on Al_2O_3 substrate by MBE to single laser pulses of: wavelength 800 nm, duration 60 fs and energy from 1.3 μJ to 4.6 μJ [38]. The energy density distributions were in the range of 22-82 mJ/cm^2.

A normalized PMOKE remanence image of the sample after irradiation measured by Kisielewski et al is shown in figure 1.4. Zero remanence corresponds to in-plane magnetic anisotropy. Non-zero remanence means that there is a remaining out-of-plane component of the vector of magnetization in zero outer field which means that the sample has PMA in the area. Colored rings are visible in the remanence picture where the sample was irradiated with a pulse. The appearance of the concentric rings is connected to the laser pulse carrying different energy density for different distances from the center of the pulse.

Measuring the spatial distribution of the energy in the pulse allows putting the energy density of the light at a specific place of the sample in connection with the observed normalized remanence at the place. A map showing the dependence of the normalized remanence on the Co layer thickness and the energy density of the incident light is shown in figure 1.5. As in the case of irradiation by Ga^+ ions two branches of induced out-of-plane magnetization are observed.

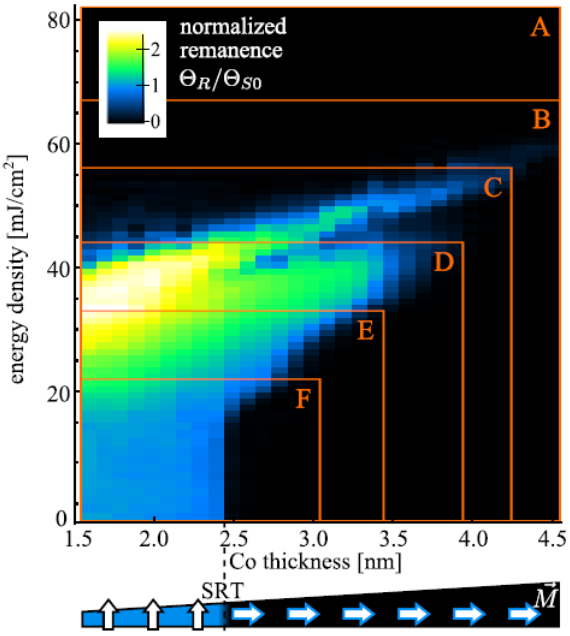

Figure 1.5: A map showing the normalized PMOKE remanence of laser irradiated Pt/Co/Pt in dependence of the thickness of the Co layer and the energy density of the incident light for the wavelength of 800 nm. The picture is taken from Ref. [38].

Atomic force microscopy (AFM) measurements of the laser spots show no change in the sample topography in the places with induced PMA [38]. The 3D time of flight secondary ion mass spectroscopy (ToF-SIMS) indicated significant diffusion of the Co atoms into both the top and the bottom Pt layers in the area of the laser spot [38]. Kisielewski et al suggest that the observed changes of the magnetic properties are due to the formation of ordered CoPt alloys induced by laser irradiation but they conclude that more experiments are needed to prove the hypothesis [38].

Similar results should be achieved by irradiation with a pulse of extreme ultraviolet radiation (EUV) because the changes of properties depend rather on the cooling process than the fast process of heating up [39]. Shorter wavelengths allow higher resolution optical lithography. Due to a difference in refraction indices the required energy density to achieve similar modifications is different to the case of infrared pulses.

Sveklo et al modified MBE grown Pt (5 nm)/Co (d_{Co})/Pt (5 nm) samples on Al_2O_3 substrates by 3 ns EUV pulses with energy densities up to 110 mJ/cm^2 [39]. The Co layer was grown in steps. The lowest d_{Co} thickness was 0.5 nm and the greatest 10 nm. All steps were 1 mm wide. The spectrum of the irradiating pulse had a peak at the wavelength of 11 nm and a wide EUV tail.

A PMOKE remanence image of a sample modified by single pulses is shown in figure 1.6. Similarly, as in the case of irradiation by infrared pulses, concentric rings can be seen in the image. For Co layer thicknesses below the SRT thickness (d_{SRT} = 2 nm for this sample) a suppression of PMA can be seen, whereas for Co layer with thicknesses equal to or greater than the SRT thickness PMA state is created for certain incident energy densities (white areas).

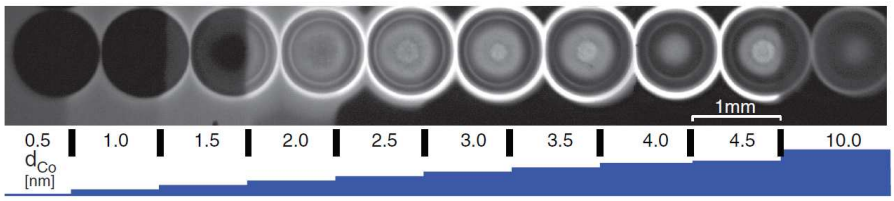

Figure 1.6: A PMOKE remanence image of Pt/Co/Pt after irradiation with single laser pulses of EUV irradiation. Black color corresponds to zero and white to non-zero remanence. The thickness of the cobalt layer varies in steps. Each pulse irradiated partly an area of the sample with one thickness and partly an area with a different one. The picture is taken from Ref. [39].

AFM images do not show substantial damage to the surface of irradiated samples for incident energy densities up to approximately 70 mJ/cm^2 [39].

Transmission electron microscopy (TEM) measurements performed on the Pt/Co/Pt trilayers repeatedly irradiated with EUV pulses with a maximal energy density of 50 mJ/cm^2 reveal significant intermixing of the Pt and Co layers [40]. XRD measurements do not indicate a creation of ordered CoPt alloys [40].

Sveklo et al suggest that the changes in magnetic properties can be attributed to residual strain after thermoplastic deformation caused by the absorption of the EUV pulse [39]. This explanation is also supported by experiments on the effects of repeated irradiation or irradiation with overlapping pulses [39]. The $CoPt_3$ disordered alloy with magnetic anisotropy [41] might also be present in the samples.

1.3.3 Reversible modification of magnetic properties

Reversible modifications of magnetic properties can be used for controlling the motion of domain walls in new spintronic devices as has been shown for example in Refs. [42, 43]. A number of methods have been suggested.

One way to go is to combine piezoelectric and magnetic materials. When the materials are grown on top of each other magnetic properties can be controlled through voltage application [44].

Also, application of a voltage across a ferromagnetic metal/oxide interface results in charge accumulation at the interface which can affect the interface magnetic anisotropy [45]. However, the observed influence on domain wall propagation is not large [46].

Bauer et al demonstrated an approach to switching magnetic properties of ferromagnetic nanostructures through ion migration in electric field [43]. Magnetic anisotropy of nanostructures with a Co/metal-oxide interface is influenced by Co-O hybridization [47]. When a good ionic conductor such as amorphous GdOx [48] is used migration of O^{2-} ions can be controlled by an electric field which affects the magnetic anisotropy.

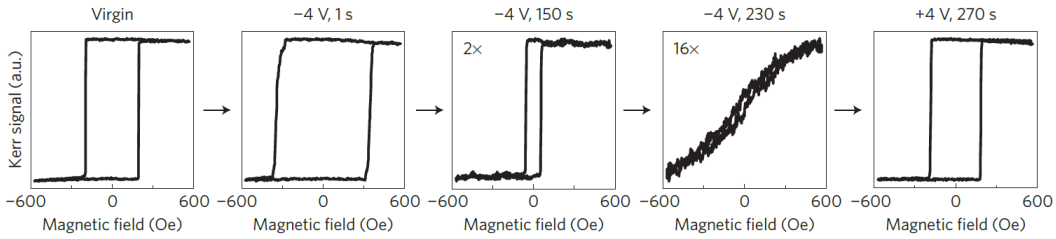

Figure 1.7: PMOKE hysteresis loops of Si/SiO_2/Ta (4 nm)/Pt (3 nm)/Co (0.9 nm)/GdOx (3 nm)/GdOx (30 nm)/Ta (2 nm)/Au (12 nm) nanostructures before and after application of negative and then positive voltage for a certain amount of time. The picture is taken from Ref. [49].

Bauer et al sputter deposited Ta (4 nm)/Pt (3 nm)/Co (0.9 nm)/GdOx (3 nm) on oxidized Si substrate. GdOx (30 nm)/Ta (2 nm)/Au (12 nm) electrodes were then deposited on this structure. Figure 1.7 shows PMOKE hysteresis loops measured on the electrodes of these samples after application of specific voltage for a certain amount of time. The as-deposited sample has out-of-plane anisotropy as can be seen from the hysteresis loop. When a negative voltage is applied (while the sample is heated to 100 °C) the coercive field increases at first but with longer modification times it reduces to zero. Zero coercive field in PMOKE corresponds to in-plane anisotropy. Upon application of +4 V for 270 s on the sample heated to 100 °C the original state is restored which shows that the induced changes are reversible.

In situ spatially resolved electron energy-loss measurements performed in TEM on samples with the same composition as above confirmed the migration of O^{2-} ions [49]. Application of negative bias for long enough time leads to the O getting as far as the bottom Pt/Co interface.

A reduction of the GdOx, Ta and Au layer thicknesses results in lower modification times at room temperature [49].

The effects of ion migration in electric field were also studied by magneto-optical spectroscopy which confirmed that the Co layer became partly oxidized after application of voltage [50].

2. Polarized light and magneto-optical observables

Magneto-optical Kerr effect is the change of polarization or intensity of reflected light when polarized light reflects from a magnetized surface. Therefore, when discussing magneto-optics it is necessary to first say something about the description of polarized light and only then define the magneto-optical Kerr effect itself.

2.1 Ellipse of polarization

Polarization is a degree of freedom of electromagnetic waves. It is determined from the vector of the intensity of electric field of the wave because electric field results in higher Lorentz force than the magnetic field of the wave.

Light is generally elliptically polarized. Special cases of polarization are linear and circular polarization.

Four parameters are needed to describe a polarization state. For a plane wave propagating in the z direction of a Cartesian coordinate system these parameters may be: the amplitude a_x and phase φ_x of the x-component of the wave and the amplitude a_y and the phase φ_y of the y-component of the wave.

When it is not important to know the exact phase of the wave at the time $t = 0$ only three parameters are enough to describe the polarization state. For the example mentioned above it can be a_x, a_y and the phase difference $\varphi = \varphi_y - \varphi_x$.

Alternatively, the parameters of the ellipse of polarization shown in figure 2.1 also give the full information about the polarization state of a plane wave propagating in the z direction.

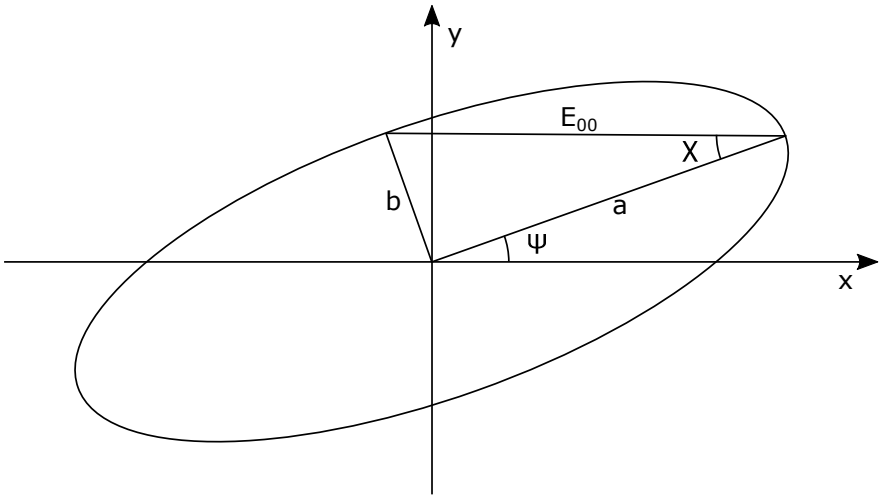

Figure 2.1: The ellipse of polarization with its parameters.

The tilt of the ellipse ψ is called the azimuth and it is an oriented angle in the interval $-\frac{\pi}{2} \leq \psi < \frac{\pi}{2}$.

The ellipticity angle χ is defined by the equation $\tan\chi = \pm\frac{b}{a}$ where a is the length of the major axis and b the length of the minor axis of the ellipse. The

ellipticity angle satisfies the condition $-\frac{\pi}{4} \leq \chi \leq \frac{\pi}{4}$. $e = \tan\chi$ is called the ellipticity. Positive sign of e is used for right-handed polarization in this work.

Finally, $E_{00} = \sqrt{a^2 + b^2}$ is the amplitude.

2.2 Jones formalism

In order to easily and effectively describe the polarization of light and its changes when light passes through polarizing optical elements, the formalism of Jones vectors and matrices has been created. Only fully polarized light can be described within this formalism.

Let us have a plane wave propagating along the z axis of a Cartesian coordinate system:

$$\vec{E} = \begin{pmatrix} a_x e^{i(\omega t - kz + \varphi_x)} \\ a_y e^{i(\omega t - kz + \varphi_y)} \\ 0 \end{pmatrix}, \tag{2.1}$$

where ω is the angular frequency of the wave and $\vec{k} = (0, 0, k)$ is the wavevector.

Jones vector is constructed by taking only the parameters which affect polarization from the first two elements of the vector in equation (2.1)

$$\vec{J} = \begin{pmatrix} A_x \\ A_y \end{pmatrix} = \begin{pmatrix} a_x e^{i\varphi_x} \\ a_y e^{i\varphi_y} \end{pmatrix}. \tag{2.2}$$

The scalar product of Jones vectors is defined as follows

$$\left(\vec{J_1}, \vec{J_2}\right) = A_{1x} A_{2x}^* + A_{1y} A_{2y}^*. \tag{2.3}$$

When the absolute phase is not important $e^{i\varphi_x}$ can be factored out from the Jones vector and omitted, leaving the following vector

$$\vec{J} = \begin{pmatrix} a_x \\ a_y e^{i\varphi} \end{pmatrix}. \tag{2.4}$$

With the definition (2.3) the scalar product of a Jones vector $\vec{J}$ with itself is proportional to the intensity of light. Often the absolute intensity is not needed so the Jones vectors are normalized to 1.

A Jones vector of light linearly polarized in a plane at an angle α with the x axis is the following

$$\vec{J}_\alpha = \begin{pmatrix} \cos\alpha \\ \sin\alpha \end{pmatrix}. \tag{2.5}$$

For right hand circular polarized (R) and left hand circular polarized(L) light we get

$$\vec{J}_{\substack{R \\ L}} = \frac{1}{\sqrt{2}} \begin{pmatrix} 1 \\ \pm i \end{pmatrix}. \tag{2.6}$$

In Jones formalism, every optical element which modifies the polarization state of the light passing through it is assigned a matrix T. To get the Jones vector $\vec{J_o}$ of the light at the output of the element the vector $\vec{J_i}$ at the input is multiplied by the matrix of the optical element

$$\vec{J_o} = T\vec{J_i}. \tag{2.7}$$

The Jones matrix of a polarizer with an easy axis at an angle β with the x axis of the coordinate system is

$$P = \begin{pmatrix} \cos^2\beta & \sin\beta\cos\beta \\ \sin\beta\cos\beta & \sin^2\beta \end{pmatrix}. \tag{2.8}$$

A waveplate characterized by retardation Γ has the following Jones matrix

$$R = \begin{pmatrix} e^{i\frac{\Gamma}{2}} & 0 \\ 0 & e^{-i\frac{\Gamma}{2}} \end{pmatrix}. \tag{2.9}$$

Materials exhibiting magneto-optical effects modify the polarization of the light too. This can be expressed by a Jones matrix. In the case of light incident on a material it is best to work in the basis of s- (perpendicular to the plane of incidence) and p- (parallel to the plane of incidence) polarizations. A general matrix of a sample in reflection geometry is

$$S = \begin{pmatrix} r_{ss} & r_{sp} \\ r_{ps} & r_{pp} \end{pmatrix}. \tag{2.10}$$

r_{ss} and r_{pp} are the reflection coefficients for s- and p-polarized light, respectively. The off-diagonal elements cause mixing of s- and p-polarized components of the incident wave and materials for which they are non-zero exhibit magneto-optical effects.

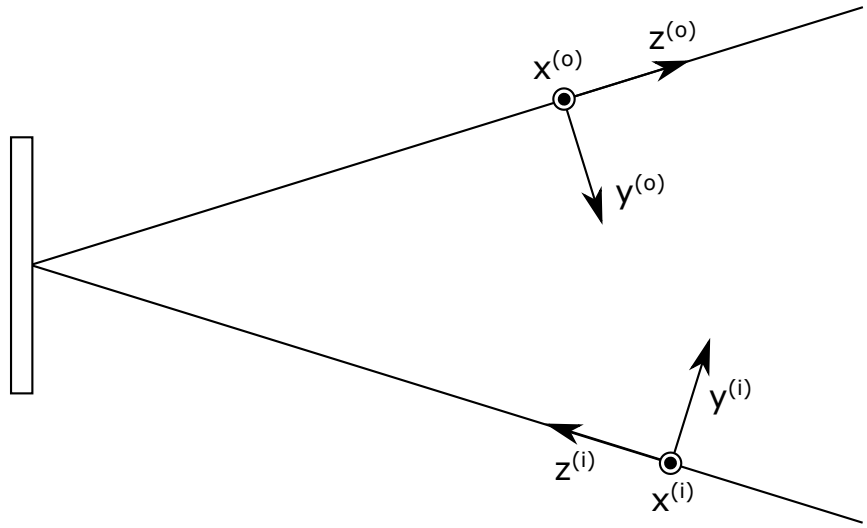

Figure 2.2: The coordination system for the incident (i) and the reflected wave (o).

When light reflects from a sample the z axis of the coordinate system of the Jones vector still has to correspond to the direction of propagation. Therefore there is a coordinate system for the incident light and another one for the reflected light as shown in figure 2.2. With this coordinate system the x axis corresponds to s-polarization and the y axis to p-polarization.

2.3 Magneto-optical observables

There are three geometries of magneto-optical experiments based on the direction of magnetization in the sample with respect to the plane of incidence of light. They are sketched in figure 2.3.

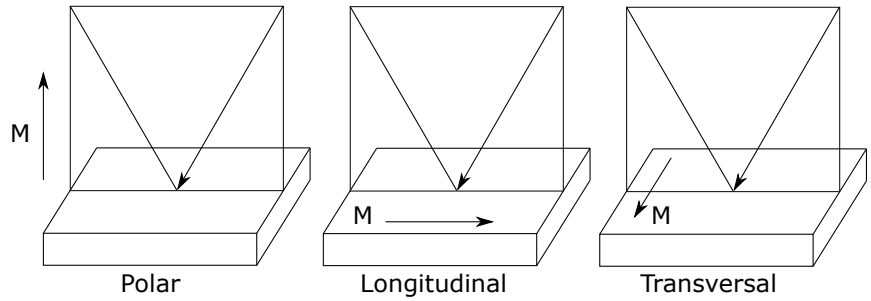

Figure 2.3: Geometries of magneto-optical experiments. M is the magnetization vector.

In polar geometry, the sample is magnetized in the direction perpendicular to its surface whereas for longitudinal and transversal geometry the vector of magnetization lies parallel to the surface. Polar magneto-optical Kerr effect (PMOKE), longitudinal magneto-optical Kerr effect (LMOKE) and transversal magneto-optical Kerr effect (TMOKE) are caused by the respective component of the magnetization vector. PMOKE and LMOKE modify the polarization of light, TMOKE changes the intensity of reflected p-polarized light as a function of the magnitude of the transversal element of magnetization.

The elements of the matrix (2.10) are not independent in the case of polar, longitudinal or transversal geometry. Taking symmetry of the problem into account the Jones matrix of the sample in polar geometry can be rewritten as [51]

$$S = \begin{pmatrix} r_{ss} & r_{sp} \\ r_{sp} & r_{pp} \end{pmatrix}. \tag{2.11}$$

The general definitions of magneto-optical Kerr effect for s- and p-polarized light are [51]

$$\Phi_{K_s} = -\frac{r_{ps}}{r_{ss}}, \tag{2.12}$$

$$\Phi_{K_p} = \frac{r_{sp}}{r_{pp}}. \tag{2.13}$$

For small magneto-optical angles the following approximation can be made [51]

$$\Phi_{K_s} \approx \theta_{K_s} - i\epsilon_{K_s}, \tag{2.14}$$

$$\Phi_{K_p} \approx \theta_{K_p} - i\epsilon_{K_p}, \tag{2.15}$$

where θ_K is the Kerr rotation and ϵ_K the Kerr ellipticity.

3. Calculations of magneto-optical effects

This work uses a comparison between a theoretical calculation of the spectral dependence of magneto-optical Kerr effect and experimental spectra to determine the profile of studied nanostructures. In order to calculate the magneto-optical spectra, we need to discuss the equations governing the propagation of light in such structures. Wave equation for propagation in an anisotropic material is written and solved and then a matrix formalism for layered anisotropic media is presented in this chapter. This formalism allows calculations of reflection coefficients which can then be used to calculate the Kerr effect.

3.1 Wave equation in anisotropic media

Electromagnetism is governed by four Maxwell's equations

$$\nabla \times \vec{E} + \frac{\partial \vec{B}}{\partial t} = 0, \tag{3.1}$$

$$\nabla \times \vec{H} - \frac{\partial \vec{D}}{\partial t} = \vec{j}, \tag{3.2}$$

$$\nabla \cdot \vec{D} = \rho, \tag{3.3}$$

$$\nabla \cdot \vec{B} = 0. \tag{3.4}$$

Let us consider a case with no sources, i.e. $\vec{j} = 0$ and $\rho = 0$. Furthermore, let us assume the validity of the following material relations

$$\vec{D} = \overleftrightarrow{\varepsilon}\varepsilon_0\vec{E}, \tag{3.5}$$

$$\vec{B} = \mu_r\mu_0\vec{H}, \tag{3.6}$$

where $\overleftrightarrow{\varepsilon}$ is the tensor of relative permittivity, ε_0 the vacuum permittivity, μ_r the relative permeability and μ_0 the vacuum permeability.

The relative permeability μ_r can be set to 1 at optical frequences [52]. Then the interaction between light and a material is given just by the permittivity tensor of the material

$$\overleftrightarrow{\varepsilon} = \begin{pmatrix} \varepsilon_{xx} & \varepsilon_{xy} & \varepsilon_{xz} \\ \varepsilon_{yx} & \varepsilon_{yy} & \varepsilon_{yz} \\ \varepsilon_{zx} & \varepsilon_{zy} & \varepsilon_{zz} \end{pmatrix}. \tag{3.7}$$

The wave equation can be derived from equations (3.1) and (3.2). For a plane wave with electric intensity $\vec{E} = \vec{E}_0 e^{i\left(\omega t - \vec{k}\cdot\vec{r}\right)}$ it takes the form [51]

$$\vec{k} \times \left(\vec{k} \times \vec{E}\right) + \frac{\omega^2}{c^2}\overleftrightarrow{\varepsilon}\vec{E} = 0, \tag{3.8}$$

where c is the speed of light in vacuum.

By the use of the identity for the triple vector product

$$\vec{a} \times (\vec{b} \times \vec{c}) = \vec{b}(\vec{a} \cdot \vec{c}) - \vec{c}(\vec{a} \cdot \vec{b}). \tag{3.9}$$

we get

$$\vec{k}\left(\vec{k}\cdot\vec{E}\right)-\vec{E}\left(\vec{k}\cdot\vec{k}\right)+\frac{\omega^2}{c^2}\overleftrightarrow{\varepsilon}\vec{E}=0. \tag{3.10}$$

It is useful to introduce the reduced wave vector

$$\vec{\bar{N}}=\vec{k}\frac{c}{\omega}. \tag{3.11}$$

The vector equation (3.10) with the use of the definition (3.11) expressed in components takes the form

$$\bar{N}_i\bar{N}_jE_j-\bar{N}_j\bar{N}_jE_i+\varepsilon_{ij}E_j=0, \tag{3.12}$$

where Einstein's summation convention is used.

The relationship (3.12) is a system of equations which can be rewritten in a matrix form while the coordinate system can be chosen in such a way that $\bar{N}_x=0$

$$\begin{pmatrix}\varepsilon_{xx}-\bar{N}_y^2-\bar{N}_z^2 & \varepsilon_{xy} & \varepsilon_{xz}\\ \varepsilon_{yx} & \varepsilon_{yy}-\bar{N}_z^2 & \varepsilon_{yz}+\bar{N}_y\bar{N}_z\\ \varepsilon_{zx} & \varepsilon_{zy}+\bar{N}_y\bar{N}_z & \varepsilon_{zz}-\bar{N}_y^2\end{pmatrix}\begin{pmatrix}E_x\\E_y\\E_z\end{pmatrix}=0. \tag{3.13}$$

If the system of equations has a nontrivial solution the determinant of the matrix is zero. Upon expressing the determinant we get a polynomial of the fourth degree. If $\bar{N}_y$ is a fixed value four solutions $\bar{N}_{zj}$ are given by the characteristic equation.

For every $\bar{N}_{zj}$ there is a corresponding solution of the wave equation (3.13) [53]

$$\vec{e}_j=\begin{pmatrix}-\varepsilon_{xy}\left(\varepsilon_{zz}-\bar{N}_y^2\right)+\varepsilon_{xz}\left(\varepsilon_{zy}+\bar{N}_y\bar{N}_{zj}\right)\\ \left(\varepsilon_{zz}-\bar{N}_y^2\right)\left(\varepsilon_{xx}-\bar{N}_y^2-\bar{N}_{zj}^2\right)-\varepsilon_{xz}\varepsilon_{zx}\\ -\left(\varepsilon_{xx}-\bar{N}_y^2-\bar{N}_{zj}^2\right)\left(\varepsilon_{zy}+\bar{N}_y\bar{N}_{zj}\right)+\varepsilon_{zx}\varepsilon_{xy}\end{pmatrix}. \tag{3.14}$$

The solutions $\vec{e}_j$ are the proper modes in the anisotropic medium which means that their polarization state does not change when propagating in the medium.

A general electric field intensity $\vec{E}$ can be expressed as a linear combination of the proper modes as

$$\vec{E}=\sum_{j=1}^{4}E_{0j}\vec{e}_je^{i\left(\omega t-\frac{\omega}{c}\vec{\bar{N}}_j\cdot\vec{r}\right)}. \tag{3.15}$$

3.2 Propagation along the magnetization vector

Let us apply the theory to a special case of light propagating in the direction of the vector of magnetization of the material now. Let the magnetization vector be oriented along the z axis of the coordinate system. In such case the permittivity tensor has the form [51]

$$\overleftrightarrow{\varepsilon}=\begin{pmatrix}\varepsilon_1 & -i\varepsilon_2 & 0\\ i\varepsilon_2 & \varepsilon_1 & 0\\ 0 & 0 & \varepsilon_3\end{pmatrix}. \tag{3.16}$$

This leads to the wave equation

$$\begin{pmatrix}\varepsilon_1-\bar{N}_y^2-\bar{N}_z^2 & -i\varepsilon_2 & 0\\ i\varepsilon_2 & \varepsilon_1-\bar{N}_z^2 & \bar{N}_y\bar{N}_z\\ 0 & \bar{N}_y\bar{N}_z & \varepsilon_3-\bar{N}_y^2\end{pmatrix}\begin{pmatrix}e_x\\e_y\\e_z\end{pmatrix}=0. \tag{3.17}$$

We are investigating the special case of light propagating along the magnetization vector, i.e. the z axis. That means that $\bar{N}_y = 0$.

The determinant of the system of equations has to be zero to obtain a non-trivial solution.

$$\begin{vmatrix} \varepsilon_1 - \bar{N}_z^2 & -i\varepsilon_2 & 0 \\ i\varepsilon_2 & \varepsilon_1 - \bar{N}_z^2 & 0 \\ 0 & 0 & \varepsilon_3 \end{vmatrix} = \left(\varepsilon_1 - \bar{N}_z^2\right)^2 \varepsilon_3 - \varepsilon_2^2 \varepsilon_3 = 0. \tag{3.18}$$

That gives the following relationship for the square of $\bar{N}_z$

$$\bar{N}_z^2 = \varepsilon_1 \pm \varepsilon_2. \tag{3.19}$$

That corresponds to squares of the complex indices of refraction for proper modes in anisotropic medium [51]

$$N_+ = \sqrt{\varepsilon_1 + \varepsilon_2} \qquad \text{and} \qquad N_- = \sqrt{\varepsilon_1 - \varepsilon_2}. \tag{3.20}$$

When the reduced wave vector $\bar{N}$ is known it is possible to calculate the proper modes by putting it into equation (3.14). The results are summed up in table 3.1.

Table 3.1: The values of $\bar{N}_z$ and the corresponding proper modes when light propagates along the magnetization vector.

$N_{z1} = N_+$	$N_{z2} = -N_+$	$N_{z3} = N_-$	$N_{z4} = -N_-$
$\vec{e}_1 = \begin{pmatrix} 1 \\ i \\ 0 \end{pmatrix}$	$\vec{e}_2 = \begin{pmatrix} 1 \\ i \\ 0 \end{pmatrix}$	$\vec{e}_3 = \begin{pmatrix} 1 \\ -i \\ 0 \end{pmatrix}$	$\vec{e}_4 = \begin{pmatrix} 1 \\ -i \\ 0 \end{pmatrix}$

From the comparison of the modes in table 3.1 with the Jones vectors in equation (2.6) it is evident that the proper modes are right hand circular polarization ($\vec{e}_1$ and $\vec{e}_1$) and left hand circular polarization ($\vec{e}_3$ and $\vec{e}_4$). The solutions with the same proper modes differ by the sign of the z-component of the reduced wave vector. That corresponds to opposite direction of propagation as can be easily seen from the definition of the reduced wave vector (3.11).

To sum the results up, when anisotropy is caused by magnetization in an originally isotropic medium and light propagates along the vector of magnetization circular polarizations become the proper modes in the medium. The complex refractive index varies between the right-hand circular polarization and the left-hand circular polarization which means that the propagation speed and the absorption also differ between these polarization states.

The special case discussed above applies to the Faraday effect and the polar Kerr effect at normal light incidence.

3.3 4×4 transfer matrix formalism for anisotropic media

Yeh developed a matrix formalism to describe the interaction of a plane wave with a layered non-absorbing medium [54]. This formalism can also be extended to absorbing media [53]. The formalism is laid out briefly in this section.

Let us consider the following situation: we have a structure with m layers. The interfaces between the layers are flat and parallel. The Cartesian coordinate system is chosen in such a way that the z axis is perpendicular to the interfaces of the layers and y-z is the plane of incidence of light. The angle of incidence is φ. The optical properties of each layer are given by $\overleftrightarrow{\varepsilon}^{(n)}$. z_n denotes the z coordinate of the interface between the nth and the the $(n+1)$th layer. The isotropic half-spaces before and after the multilayer are numbered 0 and $m+1$.

First of all, the solution of the wave equation has to be found for each layer. Thanks to the choice of the coordinate system the assumption $\bar{N}_x = 0$ used during the solving of the wave equation in section 3.1 is fulfilled. Snell's law implies that the tangential component of the wave vector is conserved at an interface. This means that $\bar{N}_y$ for all layers is equal to $\bar{N}_y$ of the incident wave which is $\bar{N}_y = |\vec{\bar{N}}^{(0)}| \sin\varphi = \frac{c}{\omega} k^{(0)} \sin\varphi = N^{(0)} \sin\varphi$ where $k^{(0)}$ is the magnitude of the wave vector of the incident wave and $N^{(0)}$ is the complex index of refraction in the half-space 0.

In the layer n there are four $\bar{N}_{zj}^{(n)}$ as shown in section 3.1. One proper mode $\vec{\bar{e}}_j^{(n)}$ corresponds to each $\bar{N}_{zj}^{(n)}$. The electric field of a plane wave in the layer n can be expressed as a superposition of these modes

$$\vec{E}^{(n)} = \sum_{j=1}^{4} E_{0j}^{(n)}(z_n)\, \vec{\bar{e}}_j^{(n)} e^{i\left[\omega t - \frac{\omega}{c}\left(\bar{N}_y y + \bar{N}_{zj}^{(n)}(z - z_n)\right)\right]}. \tag{3.21}$$

The magnetic field $\vec{B}$ can be expressed using the equation derived for a plane wave from Maxwell's equations

$$\vec{B} = \frac{1}{c} \vec{\bar{N}} \times \vec{E}. \tag{3.22}$$

Using the equations (3.22) and (3.21) we get

$$c\vec{B}^{(n)} = \sum_{j=1}^{4} E_{0j}^{(n)}(z_n)\, \vec{\bar{b}}_j^{(n)} e^{i\left[\omega t - \frac{\omega}{c}\left(\bar{N}_y y + \bar{N}_{zj}^{(n)}(z - z_n)\right)\right]}. \tag{3.23}$$

$\vec{\bar{b}}_j^{(n)}$ is the proper mode of $\vec{B}$ multiplied by the speed of light. As follows from the equation (3.22) it is equal to

$$\vec{\bar{b}}_j^{(n)} = \begin{pmatrix} 0 \\ \bar{N}_y \\ \bar{N}_{zj}^{(n)} \end{pmatrix} \times \vec{\bar{e}}_j^{(n)}. \tag{3.24}$$

Boundary conditions for electric and magnetic field allow to link the electric and magnetic fields at different layers. The tangential component of electric field is continuous at an interface. The same is true for $\vec{B}$ when there are no free surface currents at the interface. Let us assume the condition is fulfilled. The following system of equations describes the requirement of the continuity of

tangential components of $\vec{E}$ and $\vec{B}$ at the interface between layers $n-1$ and n

$$\sum_{j=1}^{4} E_{0j}^{(n-1)}\left(z_{n-1}\right) \vec{e}_j^{(n-1)} \cdot \vec{i}_x = \sum_{j=1}^{4} E_{0j}^{(n)}\left(z_n\right) \vec{e}_j^{(n)} \cdot \vec{i}_x e^{i\frac{\omega}{c}\bar{N}_{zj}^{(n)} t_n}, \tag{3.25}$$

$$\sum_{j=1}^{4} E_{0j}^{(n-1)}\left(z_{n-1}\right) \vec{b}_j^{(n-1)} \cdot \vec{i}_y = \sum_{j=1}^{4} E_{0j}^{(n)}\left(z_n\right) \vec{b}_j^{(n)} \cdot \vec{i}_y e^{i\frac{\omega}{c}\bar{N}_{zj}^{(n)} t_n}, \tag{3.26}$$

$$\sum_{j=1}^{4} E_{0j}^{(n-1)}\left(z_{n-1}\right) \vec{e}_j^{(n-1)} \cdot \vec{i}_y = \sum_{j=1}^{4} E_{0j}^{(n)}\left(z_n\right) \vec{e}_j^{(n)} \cdot \vec{i}_y e^{i\frac{\omega}{c}\bar{N}_{zj}^{(n)} t_n}, \tag{3.27}$$

$$\sum_{j=1}^{4} E_{0j}^{(n-1)}\left(z_{n-1}\right) \vec{b}_j^{(n-1)} \cdot \vec{i}_x = \sum_{j=1}^{4} E_{0j}^{(n)}\left(z_n\right) \vec{b}_j^{(n)} \cdot \vec{i}_x e^{i\frac{\omega}{c}\bar{N}_{zj}^{(n)} t_n}, \tag{3.28}$$

where $\vec{i}_x$ and $\vec{i}_y$ are the unity vectors in the direction of the respective axes of the coordinate system.

The set of equations can be rewritten in a matrix form

$$D^{(n-1)} E_0^{(n-1)}\left(z_{n-1}\right) = D^{(n)} P^{(n)} E_0^{(n)}\left(z_n\right). \tag{3.29}$$

$D^{(n)}$ is called the dynamical matrix and has the form

$$D^{(n)} = \begin{pmatrix} \vec{e}_1^{(n)} \cdot \vec{i}_x & \vec{e}_2^{(n)} \cdot \vec{i}_x & \vec{e}_3^{(n)} \cdot \vec{i}_x & \vec{e}_4^{(n)} \cdot \vec{i}_x \\ \vec{b}_1^{(n)} \cdot \vec{i}_y & \vec{b}_2^{(n)} \cdot \vec{i}_y & \vec{b}_3^{(n)} \cdot \vec{i}_y & \vec{b}_4^{(n)} \cdot \vec{i}_y \\ \vec{e}_1^{(n)} \cdot \vec{i}_y & \vec{e}_2^{(n)} \cdot \vec{i}_y & \vec{e}_3^{(n)} \cdot \vec{i}_y & \vec{e}_4^{(n)} \cdot \vec{i}_y \\ \vec{b}_1^{(n)} \cdot \vec{i}_x & \vec{b}_2^{(n)} \cdot \vec{i}_x & \vec{b}_3^{(n)} \cdot \vec{i}_x & \vec{b}_4^{(n)} \cdot \vec{i}_x \end{pmatrix}. \tag{3.30}$$

The matrix

$$P_{ij}^{(n)} = \delta_{ij} e^{i\frac{\omega}{c}\bar{N}_{zj}^{(n)} t_n} \tag{3.31}$$

is the propagation matrix and $t_n = z_n - z_{n-1}$.

Finally, $E_0^{(n)}\left(z_n\right)$ is a column vector with $E_{0j}^{(n)}\left(z_n\right)$ as the elements.

The equation (3.29) can be multiplied by the inverse matrix of $D^{(n-1)}$ from the left and a transfer matrix $T_{n-1,n}$ can be defined.

$$E_0^{(n-1)}\left(z_{n-1}\right) = \left(D^{(n-1)}\right)^{-1} D^{(n)} P^{(n)} E_0^{(n)}\left(z_n\right) = T_{n-1,n} E_0^{(n)}\left(z_n\right). \tag{3.32}$$

We have achieved to link the coefficients E_0 at two interfaces by a matrix. If the process is repeated for all the layers it is possible to write a relationship between the coefficients at the top and bottom surface of the multilayer

$$E_0^{(0)}\left(z_0\right) = \left(\prod_{n=1}^{m+1} T_{n-1,n}\right) E_0^{(m+1)}\left(z_m\right) = M E_0^{(m+1)}\left(z_m\right), \tag{3.33}$$

where a matrix M was defined.

3.4 Isotropic layers

Multilayers often contain some isotropic layers. Even when they do not the matrix formalism in section 3.3 supposes two isotropic half-spaces so it is important to solve the wave equation for an isotropic case too. The tensor of permittivity of an isotropic layer is diagonal and the elements are equal to $\varepsilon_{ii}^{(n)} = \varepsilon_1^{(n)} = N^{(n)2}$ where $N^{(n)}$ is the complex refractive index of the layer.

The solution (3.14) of the wave equation is only valid for anisotropic media as for an isotropic material it gives a zero vector. A different solution has to be found for isotropic layers. We will make the same assumptions as we did in the case of solving the wave equation for the anisotropic layers, i.e. $\bar{N}_x = 0$ and $\bar{N}_y$ is fixed. In such a case the wave vector can be written as

$$\vec{k}_{1,2}^{(n)} = \frac{\omega}{c} \begin{pmatrix} 0 \\ \bar{N}_y \\ \pm Q^{(n)} \end{pmatrix}, \tag{3.34}$$

where $Q^{(n)}$ is a parameter.

The magnitude of the wave vector can be expressed as

$$k^{(n)} = \sqrt{\vec{k}_{1,2}^{(n)} \cdot \vec{k}_{1,2}^{(n)}} = \frac{\omega}{c} \sqrt{\bar{N}_y^2 + Q^{(n)^2}}. \tag{3.35}$$

Modifying the equation gives the following relationship for the parameter $Q^{(n)}$

$$Q^{(n)} = \sqrt{\frac{c^2}{\omega^2} k^{(n)^2} - \bar{N}_y^2} = \sqrt{N^{(n)^2} - \bar{N}_y^2}. \tag{3.36}$$

We have found the values of the z-component of the reduced wave vector, $\bar{N}_{zj}^{(n)} = \pm Q^{(n)}$. The proper modes can be chosen in a way to suit the problem [53]. One possible choice is for example s- and p-polarizations. When the proper modes are chosen the dynamical matrix of the isotropic layer can be constructed.

3.5 Reflection coefficients

Let us assume the following situation to calculate the reflection coefficients. The wave incident on the multilayer from the half-space 0 is a superposition of two ortogonal polarizations $\vec{e}_1^{(0)}$ and $\vec{e}_3^{(0)}$ with amplitudes $E_{01}^{(0)}(z_0)$ and $E_{03}^{(0)}(z_0)$. The polarizations $\vec{e}_2^{(0)}$ and $\vec{e}_4^{(0)}$ propagate in the opposite direction than $\vec{e}_1^{(0)}$ and $\vec{e}_3^{(0)}$. No light shines on the multilayer from the half-space $(m+1)$. Therefore we have the following condition

$$E_{02}^{(m+1)}(z_m) = E_{04}^{(m+1)}(z_m) = 0. \tag{3.37}$$

The relation (3.33) then takes the form

$$\begin{pmatrix} E_{01}^{(0)}(z_0) \\ E_{02}^{(0)}(z_0) \\ E_{03}^{(0)}(z_0) \\ E_{04}^{(0)}(z_0) \end{pmatrix} = \begin{pmatrix} M_{11} & M_{12} & M_{13} & M_{14} \\ M_{21} & M_{22} & M_{23} & M_{24} \\ M_{31} & M_{32} & M_{33} & M_{34} \\ M_{41} & M_{42} & M_{43} & M_{44} \end{pmatrix} \begin{pmatrix} E_{01}^{(m+1)}(z_m) \\ 0 \\ E_{03}^{(m+1)}(z_m) \\ 0 \end{pmatrix}. \tag{3.38}$$

From this equation the coefficients of reflection can be expressed

$$r_{12} = \left(\frac{E_{02}^{(0)}(z_0)}{E_{01}^{(0)}(z_0)} \right)_{E_{03}^{(0)}(z_0)=0} = \frac{M_{21}M_{33} - M_{23}M_{31}}{M_{11}M_{33} - M_{13}M_{31}}, \tag{3.39}$$

$$r_{14} = \left(\frac{E_{04}^{(0)}(z_0)}{E_{01}^{(0)}(z_0)} \right)_{E_{03}^{(0)}(z_0)=0} = \frac{M_{41}M_{33} - M_{43}M_{31}}{M_{11}M_{33} - M_{13}M_{31}}, \tag{3.40}$$

$$r_{34} = \left(\frac{E_{04}^{(0)}(z_0)}{E_{03}^{(0)}(z_0)} \right)_{E_{01}^{(0)}(z_0)=0} = \frac{M_{11}M_{43} - M_{41}M_{13}}{M_{11}M_{33} - M_{13}M_{31}}, \tag{3.41}$$

$$r_{32} = \left(\frac{E_{02}^{(0)}(z_0)}{E_{03}^{(0)}(z_0)} \right)_{E_{01}^{(0)}(z_0)=0} = \frac{M_{11}M_{23} - M_{21}M_{13}}{M_{11}M_{33} - M_{13}M_{31}}. \tag{3.42}$$

3.6 Polar Kerr effect at normal light incidence

When we investigate polar Kerr effect at normal light incidence the electromagnetic wave travels along the magnetization vector. The wave equation was solved for this case in section 3.2 and it was shown that the circular polarizations are the proper modes.

$$\vec{e}_1^{(n)} = \vec{e}_2^{(n)} = \frac{1}{\sqrt{2}} \begin{pmatrix} 1 \\ i \\ 0 \end{pmatrix} \qquad \text{and} \qquad \vec{e}_3^{(n)} = \vec{e}_4^{(n)} = \frac{1}{\sqrt{2}} \begin{pmatrix} 1 \\ -i \\ 0 \end{pmatrix}. \tag{3.43}$$

With the knowledge of $\bar{N}_{zj}^{(n)}$ and the proper modes $\vec{e}_j^{(n)}$ the dynamical matrix $D^{(n)}$ for the nth layer, the inverse dynamical matrix $D^{(n-1)}$ for the $(n-1)$st layer and the propagation matrix can be constructed. When the matrices are multiplied in the same order as in (3.32) the transfer matrix $T_{n-1,n}$ is found. As derived in Ref. [51] the transfer matrix is block diagonal with 2×2 blocks. The M matrix is a product of transfer matrices therefore it is block diagonal too:

$$M = \begin{pmatrix} M_{11} & M_{12} & 0 & 0 \\ M_{21} & M_{22} & 0 & 0 \\ 0 & 0 & M_{33} & M_{34} \\ 0 & 0 & M_{43} & M_{44} \end{pmatrix} \tag{3.44}$$

The equation (3.39) then gives the following reflection coefficient of the right hand circularly polarized light

$$r_+ = \frac{M_{21}}{M_{11}}. \tag{3.45}$$

Similarly, we get for the left hand circularly polarized light from equation (3.41)

$$r_- = \frac{M_{43}}{M_{33}}. \tag{3.46}$$

Polar Kerr rotation and ellipticity can be calculated from [51]

$$\theta_K = \frac{1}{2} \arg \frac{r_-}{r_+}, \tag{3.47}$$

$$\epsilon_K = \frac{|r_-| - |r_+|}{|r_-| + |r_+|}. \tag{3.48}$$

The derivation here was done for the special case of normal incidence of light but the same formalism can be used to calculate the Kerr effect at a general angle of incidence.

4. Experimental methods

Magneto-optical and optical methods are used in this work. These methods are nondestructive and have in-depth sensitivity hence they are also sensitive to interfaces in nanostructures.

Magneto-optical spectroscopy is a powerful tool for studying nanostructures with magnetic layers. Some materials are studied because of the magneto-optical properties themselves. This is the case of materials with possible applications in new 3D screens or for use in integrated photonic non-reciprocal devices where the amplitude of Kerr or Faraday rotation is important.

Also, off-diagonal components of the permittivity tensor can be calculated from measured magneto-optical spectra when the diagonal components are known. Upon doing that the whole information to describe the material's optical response is known (assuming that $\mu = \mu_0$).

Last but not least, magneto-optical spectroscopy provides a way to study changes in magnetic materials which is the way it is employed in this work.

Magneto-optical methods can be divided into two groups: methods measuring intensity and modulation techniques [51].

One of the intensity methods is the differential intensity detection method where a polarization bridge is used to decompose the light reflected from the sample into two spatially separated beams with orthogonal polarizations. The intensity of each of the beams is measured. This technique is often used for measurements of hysteresis loops.

Another method based on measuring the intensity of light is the rotating analyzer method which was used for measurements of Kerr spectra in this work. It is explained in greater detail further in this chapter.

The modulation techniques either modulate the azimuth or the ellipticity of the polarized light beam used for measurement. They are discussed for example in Ref. [51].

From the optical methods, spectroscopic ellipsometry which allows the determination the diagonal elements of the permittivity tensor from measuring the change of polarization upon reflection from a sample is laid out here.

4.1 Magneto-optical spectroscopy: rotating analyzer method

A diagram of the rotating analyzer apparatus is shown in figure 4.1. Light is collimated by a lens, passes through a polarizer, is focused on the sample magnetized in the out-of-plane direction, reflects from it, gets collimated again, goes through waveplates and an analyzer which can rotate and finally is focused to a detector.

The intensity measured by the detector can be calculated using the Jones matrix formalism. Let us assume that the polarizer is oriented in such a way that the passing light is p-polarized. In that case the Jones vector at the output of

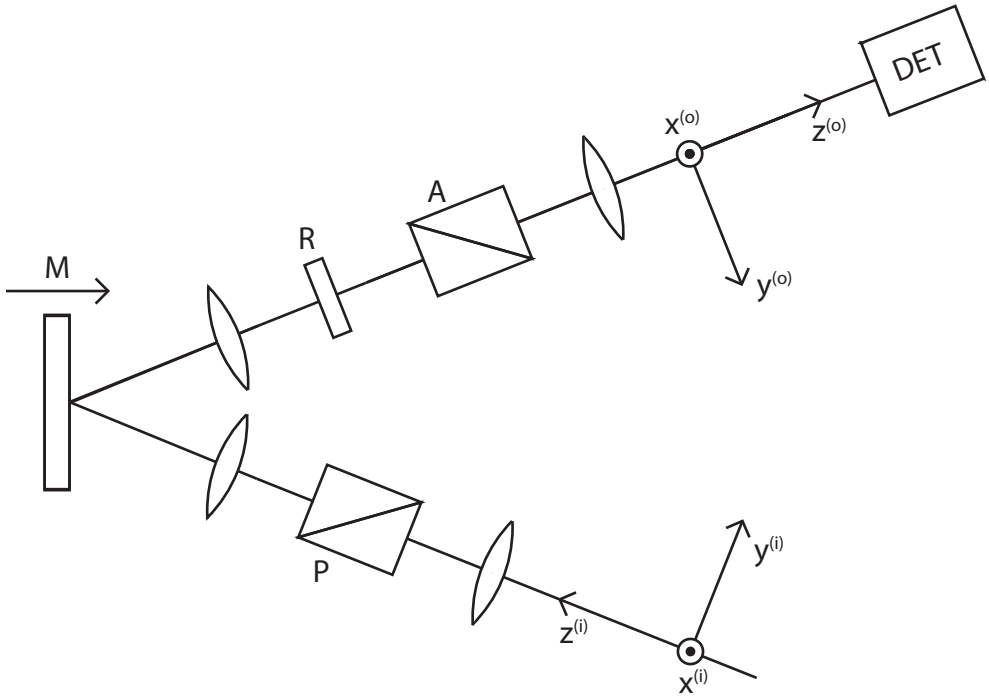

Figure 4.1: A diagram of the setup for measuring PMOKE spectra by the rotating analyser method. P stands for a polarizer, R for a retarder, A for an analyser and DET for a detector. M denotes the direction of the magnetization of a sample.

the apparatus is equal to

$$\vec{J}_o = \begin{pmatrix} \cos^2\alpha & \sin\alpha\cos\alpha \\ \sin\alpha\cos\alpha & \sin^2\alpha \end{pmatrix} \begin{pmatrix} e^{i\frac{\Gamma}{2}} & 0 \\ 0 & e^{-i\frac{\Gamma}{2}} \end{pmatrix} \begin{pmatrix} r_{ss} & r_{sp} \\ r_{ps} & r_{pp} \end{pmatrix} \begin{pmatrix} 0 \\ 1 \end{pmatrix}$$
$$= \begin{pmatrix} r_{sp}e^{i\frac{\Gamma}{2}}\cos^2\alpha + r_{pp}e^{-i\frac{\Gamma}{2}}\sin\alpha\cos\alpha \\ r_{sp}e^{i\frac{\Gamma}{2}}\sin\alpha\cos\alpha + r_{pp}e^{-i\frac{\Gamma}{2}}\sin^2\alpha \end{pmatrix}, \quad (4.1)$$

where α is the angle of the turning of the analyser and Γ is the relative phase difference between the ordinary and extraordinary beam gained in the waveplate. The angle $\alpha = 0$ corresponds to the closed position of the analyser, i.e. if the polarizer and the analyser were directly after each other no light would be transmitted for $\alpha = 0$.

The intensity of the light can be calculated as

$$I \propto |\vec{J}_o|^2 = |r_{sp}|^2\cos^2\alpha + |r_{pp}|^2\sin^2\alpha + r_{sp}r_{pp}^* e^{i\Gamma}\sin\alpha\cos\alpha + r_{sp}^* r_{pp}e^{-i\Gamma}\sin\alpha\cos\alpha. \quad (4.2)$$

This relation can be further rewritten with the definition of Kerr effect for p-polarized light (2.13)

$$I \propto |r_{pp}|^2\left[|\Phi_{K_p}|^2\cos^2\alpha + \sin^2\alpha + \sin 2\alpha\,\Re(\Phi_{K_p}e^{i\Gamma})\right]. \quad (4.3)$$

Because the Kerr effect is usually small the first term can be omitted. The use of the definition (2.15) then leads to the final relation

$$I \propto |r_{pp}|^2\left[\sin^2\alpha + \sin 2\alpha\left(\theta_{K_p}\cos\Gamma + \epsilon_{K_p}\sin\Gamma\right)\right]. \quad (4.4)$$

When the intensity I at the output of the apparatus is measured as a function of the angle α without waveplates Kerr rotation θ_{K_p} can be determined by fitting the measured dependence with the relation (4.4). Kerr ellipticity ϵ_{K_p} can then be extracted from the measurement with waveplates with a specific Γ for each wevelength. $\Gamma = \pi$ would be ideal because that way the ellipticity ϵ_{K_p} could be fitted directly from the measurement. However, it is not possible to make waveplates with $\Gamma = \pi$ for a wide spectral range. Therefore the term $\left(\theta_{K_p} \cos\Gamma + \epsilon_{K_p} \sin\Gamma\right)$ is fitted and the ellipticity ϵ_{K_p} is calculated using the rotation θ_{K_p} determined from the measurement without the retarder.

A rotating analyzer apparatus built for measurements with high spatial resolution is shown in figure 4.2.

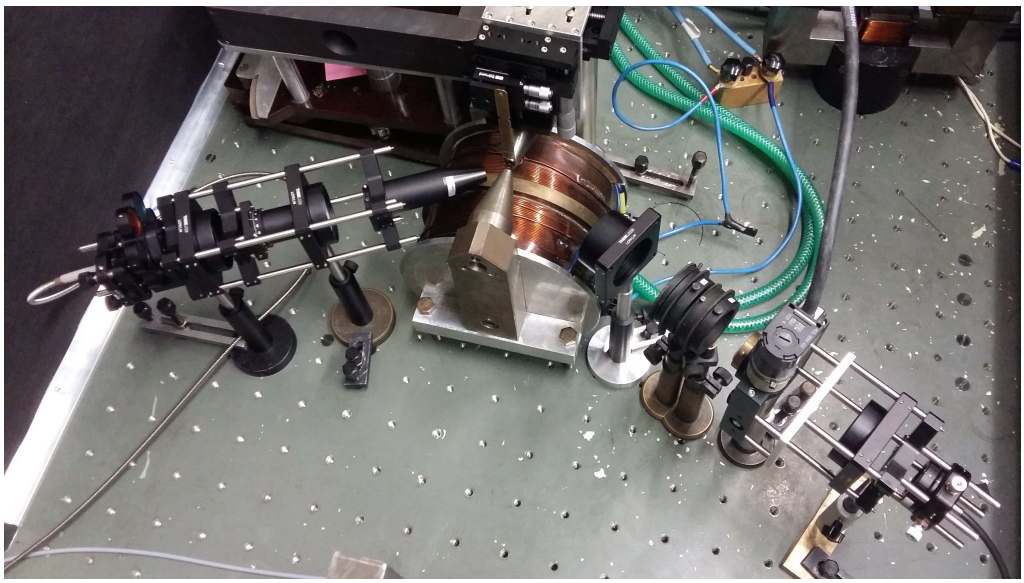

Figure 4.2: Apparatus built for measurements with high spatial resolution.

Light from a 150 W Xe lamp is brought to the apparatus by a fiber. In addition to figure 4.1 there are spectral filters between the waveguide and the collimating lens. The whole spectral region from 1.2 eV to 5 eV covered by this apparatus is measured in four parts. The spectral filters are there to prevent higher diffraction orders of the grating in the spectrometer from influencing the measurements.

Both the polarizer and the analyzer were Rochon type polarizers made of α-BBO.

All of the PMOKE spectra presented in this work were measured for p-polarized light. P-polarization was set by turning the polarizer in such a way that the reflection of light incident on a piece of glass under Brewster angle disappeared.

A focusing probe from the J. A. Woollam RC2 spectroscopic ellipsometer was used for focusing the light beam on the sample. Figure 4.3 shows the size of the spot in comparison to the size of the sample which was $1\,\mathrm{cm} \times 1\,\mathrm{cm}$.

The sample was mounted on an x-y translation stage with micrometric screws to allow precise manipulation with the position of the sample. The sample was placed in a gap of an electromagnet's magnetic circuit. The electromagnet was able to produce a maximal magnetic field of 682 mT in the gap.

Figure 4.3: The 1 cm × 1 cm sample and the spot in its bottom left corner.

The analyzer was mounted in a motor allowing to turn it by a motor controller connected to the computer. The smallest step of the motor was 1 mdeg.

After passing through the analyzer the light was focused by a lens to an optical fiber leading to a Shamrock SR-303i-B spectrometer. This spectrometer was equipped with three diffraction gratings and its chip could be cooled down to -90 °C which lowered the dark current.

PMOKE is usually measured at normal incidence or a very small angle of incidence. The rather unusual angle of incidence (64.5 deg) which was used for the apparatus in figure 4.2 was used because a high spatial resolution was needed but, at the same time, the samples had a rather high saturation field. Other strong electromagnets in our laboratory did not allow the focusing lens to be close enough to the sample to achieve the desired spatial resolution.

Samples which were not patterned and hence did not need focusing were measured by the same setup with the focusing lens removed. Also, a different electromagnet with field up to 1.2 T was used and the angle of incidence was nearly normal.

4.2 Spectroscopic ellipsometry

The Fresnel coefficients generally vary for an s- and a p-polarized wave. Therefore, when light with both s- and p-components of polarization reflects from (or transmits through) a sample its polarization generally changes. Measurement of these changes can then give information about the optical constants of the sample and the thicknesses of the layers [55].

All spectroscopic ellipsometers need a polarization generator and a polarization analyzer. These are, based on the configuration, constructed of polarizers, compensators and phase modulators [56].

A demonstration of the principle of ellipsometric measurements is done for the rotating analyzer configuration in the following text. A diagram of an ellipsometer with such configuration is in figure 4.4.

The polarization of light after passing through a polarizer oriented at an angle

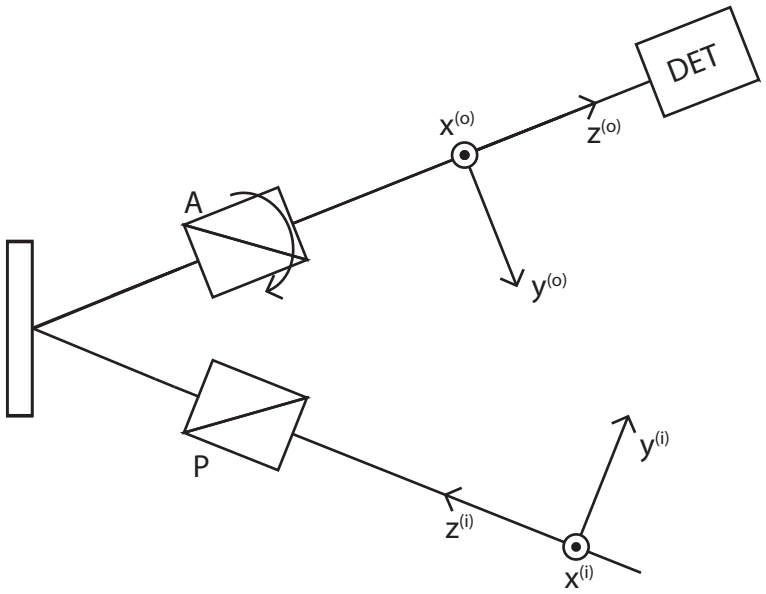

Figure 4.4: A diagram of a spectroscopic ellipsometer with a rotating analyser. P stands for the polariser, A for the analyser, DET for the detector.

α, reflecting from a sample and going through an analyser oriented at an angle θ can be calculated by multiplying the Jones vector of light polarized in the same direction as the orientation of the first polarizer by Jones matrices of a sample (with zero off-diagonal elements because the sample is not magnetized) and a polarizer.

$$\vec{J}_o = \begin{pmatrix} \cos^2\theta & \sin\theta\cos\theta \\ \sin\theta\cos\theta & \sin^2\theta \end{pmatrix} \begin{pmatrix} r_s & 0 \\ 0 & r_p \end{pmatrix} \begin{pmatrix} \cos\alpha \\ \sin\alpha \end{pmatrix} = \begin{pmatrix} r_s\cos\alpha\cos^2\theta + r_p\sin\alpha\sin\theta\cos\theta \\ r_s\cos\alpha\sin\theta\cos\theta + r_p\sin\alpha\sin^2\theta \end{pmatrix} \quad (4.5)$$

The intensity I measured by the detector can be derived from $\vec{J}_o$ as

$$I \propto |\vec{J}_o|^2 = |r_s|^2\cos^2\alpha\cos^2\theta + |r_p|^2\sin^2\alpha\sin^2\theta + \frac{1}{4}\left(r_s r_p^* + r_s^* r_p\right)\sin 2\alpha\sin 2\theta. \quad (4.6)$$

In ellipsometry it is usually the parameters Ψ and Δ which are used to describe the change in polarization. These parameters are defined by the following relation [55]

$$\rho = \frac{r_p}{r_s} \equiv \tan\Psi e^{i\Delta}. \quad (4.7)$$

The relation (4.6) can be rewritten with the definition (4.7) into the form [55]

$$I \propto 1 + \eta\sin 2\theta + \xi\cos 2\theta. \quad (4.8)$$

The parameters η and ξ are defined as follows [55]

$$\eta = 2\frac{\tan\alpha\tan\Psi\cos\Delta}{1+\tan^2\alpha\tan^2\Psi} \qquad \text{a} \qquad \xi = \frac{1-\tan^2\alpha\tan^2\Psi}{1+\tan^2\alpha\tan^2\Psi}. \quad (4.9)$$

From the measurement with a rotating analyser the intensity I is known as a function of the angle θ. The parameters η and ξ from the equation (4.8) can

be fitted from the measured dependence. Ψ and Δ can be calculated from the equations (4.9) because the angle α is known.

When only a single reflection can be taken into account the relation (4.7) can be inverted so that it gives the optical constants ε. However, even for bulk materials often a thin surface layer of oxide or roughness is present. In such a case the inversion of an equation for single reflection gives pseudo optical constants [56]

$$\langle\widetilde{\varepsilon}\rangle = \sin^2\vartheta_i \left[1 + \tan^2\vartheta_i \left(\frac{1-\rho}{1+\rho}\right)^2\right], \tag{4.10}$$

where ϑ_i is the angle of incidence.

To determine the optical constants of a layered structure (or the bulk material with a surface layer) the exact equations for reflection at a multilayer structure have to be used. Such an equation is difficult to invert so the optical constants and thicknesses of the individual layers are determined by regression.

Instead of fitting the measured Ψ and Δ with the complex permittivity (or the complex index of refraction) for each wavelength various relations for describing the spectral dependence of these properties can be used.

The Cauchy relationship can be used to describe materials which do not absorb [56]:

$$n(\lambda) = A + \frac{B}{\lambda^2} + \frac{C}{\lambda^4}, \tag{4.11}$$

where A, B and C are parameters. The relationship does not force Kramers-Kronig consistency [56].

Absorbing regions are often modeled by oscillators [56]. Absorption is parametrized by amplitude, broadening and central energy.

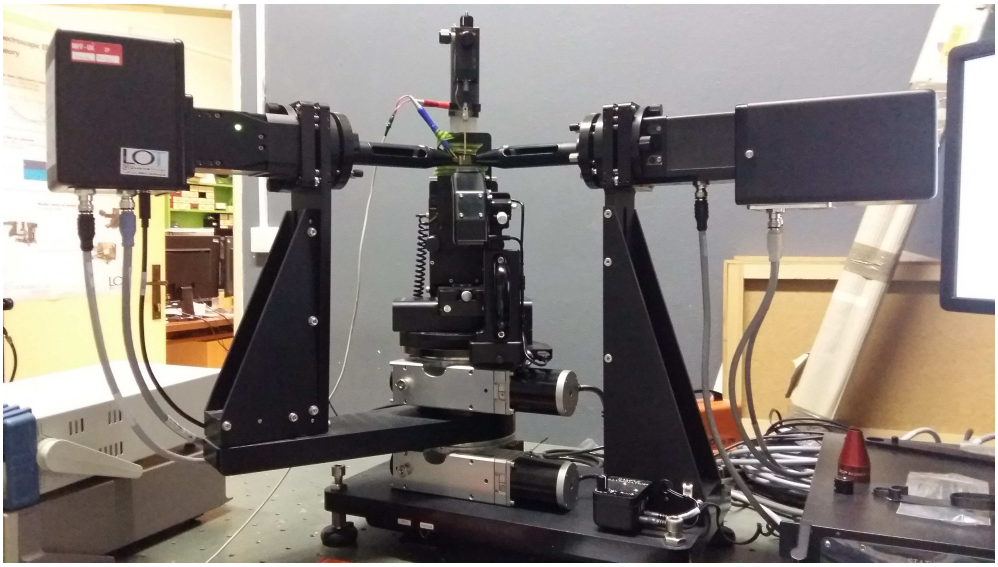

Figure 4.5: Spectroscopic ellipsometer J. A. Woollam RC2 modified for *in situ* measurements of voltage induced changes of optical properties with high spatial resolution.

Spectroscopic ellipsometer J. A. Woollam RC2 was used for measurements. Focusing probes and translation stage were used to measure with high spatial resolution. The studied sample had one bottom and a number of top electrodes. A silver wire was attached to the bottom electrode by silver paste. An add-on with a Signatone micropositioner was designed and mounted on the ellipsometer to allow application of voltage to the small top electrodes. A camera was used during contacting the top electrodes and to check where the light beam spot was on the sample. The photo of the apparatus is in figure 4.5.

5. Studied samples

The compositions and the methods of preparation of the samples studied in this work are described in this chapter.

5.1 Pt/Co/Pt trilayers irradiated with soft X-rays

Two sets of samples were grown by molecular beam epitaxy (MBE) on annealed $Al_2O_3(0001)$ substrates at the Institute of Physics of Polish Academy of Sciences. The sets only differed by the temperature of the substrate during the deposition of the bottom Pt layer. The substrate was not heated for set A and was heated to 750 °C for set B. For set B, the substrate with the bottom Pt layer was cooled down before the deposition process continued.

The structure of the samples and the thicknesses of the layers are shown in figure 5.1.

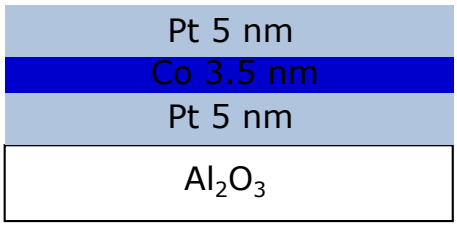

Figure 5.1: The structure of the samples on which the studies of the effects of irradiation by soft X-rays were performed.

Prague Asterix Laser System [57] was used to pump a Xe puff target [58] taken from the Military University of Technology in Warsaw, Poland. The spectrum of the emitted radiation had a peak at the wavelength of 10-11 nm and an extreme ultraviolet tail up to 70 nm. The radiation was focused by an ellipsoidal mirror. Samples were irradiated by a single pulse of approximate duration 400 ps. Each sample was irradiated homogeneously by a single energy density. The energy densities varied between 15 and 54 mJ/cm^2.

Magneto-optical remanence images show high homogeneity of modification of all of the studied samples (not shown).

5.2 Samples irradiated with Ga^+ ions

Samples of two different compositions were prepared by MBE at the Institute of Physics of Polish Academy of Sciences:

- $Al_2O_3(0001)$/Pt (20 nm)/Co (3 nm)/Pt (5 nm),
- $Al_2O_3(0001)$/Pt (20 nm)/Au (20 nm)/Co (3 nm)/Au (5 nm).

These samples were irradiated by 30 keV Ga^+ ions in 0.9 mm wide stripes at Helmholtz-Zentrum Dresden-Rossendorf in Germany. Each stripe was irradiated

by different ion fluence. The fluences varied between 5×10^{12} ions/cm^2 and 1×10^{16} ions/cm^2. One stripe for each composition was left non-irradiated and was used as a reference.

5.3 Samples for studying the effects of ion migration in electric field on optical properties

The structure of the samples for measuring the changes of optical properties induced by ion migration in an electric field is shown in figure 5.2. The samples were prepared at the Department of Materials Science and Engineering, Massachusetts Institute of Technology, USA. D. c. magnetron sputtering at room temperature was used to prepare the Ta, Pt and Au layers. The deposition was done under 3 mtorr Ar pressure with a background pressure of 1×10^{-7} torr. Reactive sputtering at an oxygen partial pressure 5×10^{-5} torr was used to deposit the GdOx layer. The top Au electrodes with a diameter of 200 μm were sputtered through a shadow mask.

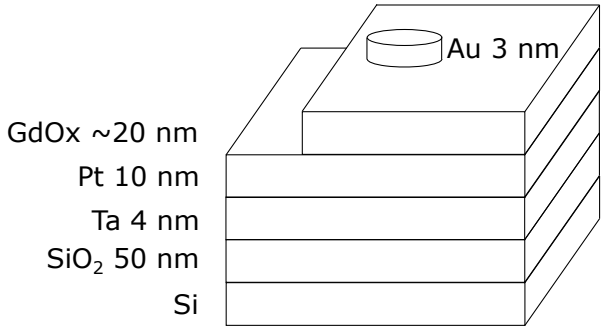

Figure 5.2: The structure of the sample for the measurements of the induced changes of optical properties. The Au layer is used as the top and the Pt layer as the bottom electrode.

6. Results

The results of optical and magneto-optical measurements of the samples described in chapter 5 are presented in this chapter. It is divided into 4 sections. The first one presents measurements of optical constants of Al_2O_3 which was used as a substrate for the majority of the sample sets. The division into the other sections is based on the studied method of modification.

6.1 Permittivity of Al_2O_3

Spectroscopic ellipsometry was used to measure the permittivity of non-annealed and annealed $Al_2O_3(0001)$ monocrystals. The knowledge of the optical constants is important because $Al_2O_3(0001)$ was used as the substrate for the majority of the studied samples. Because of the low thickness of the layers grown on the substrates (especially in the case of the samples modified by soft X-rays) the light gets all the way to the substrate and hence its permittivity can significantly influence the calculated magneto-optical response of the samples.

The spectral dependence of ellipsometric angles Ψ and Δ was measured for each sample for three angles of incidence - 55 deg, 60 deg and 65 deg. The Cauchy relationship was used to fit the experimental data.

The fitted real part of permittivity for the non-annealed substrate is shown in figure 6.1. ϵ_r for the annealed substrate is in figure 6.2. For both samples the imaginary part of permittivity was fitted as zero, corresponding to zero absorption in the studied spectral region.

The graphs 6.1 and 6.2 are nearly identical which means that annealing does not notably affect the optical properties of Al_2O_3.

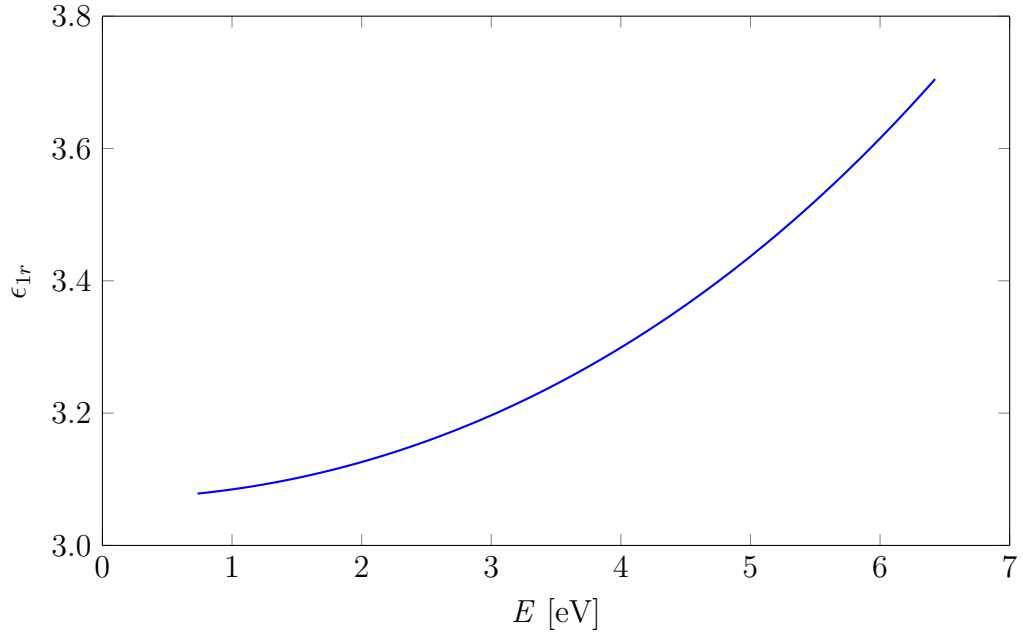

Figure 6.1: The spectral dependence of the real part of permittivity of non-annealed $Al_2O_3(0001)$.

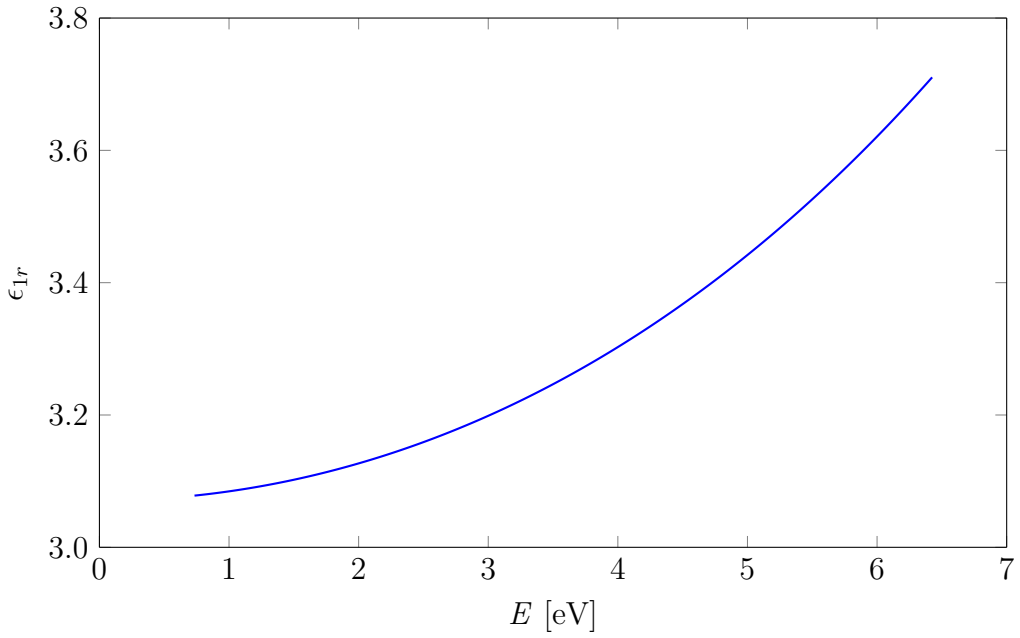

Figure 6.2: The spectral dependence of the real part of permittivity of annealed $Al_2O_3(0001)$.

6.2 Modification by a pulse of soft X-rays

In this section, the samples from set A will sometimes be labeled with "RT" indicating that the substrate was not heated during the growth of the bottom Pt layer. Similarly, the samples from set B will be labeled "750 °C".

6.2.1 Non-irradiated Pt/Co/Pt samples

Samples prepared in the same deposition round as the samples which were later irradiated were used as a reference. Measurements of the reference samples firstly allow to compare the properties of the nanostructures before and after modification and secondly can be used to calculate the optical and magneto-optical constants of Co which can then be used in models of the irradiated samples.

Polar Kerr rotation hysteresis loops measured on the reference samples at the photon energy 1.94 eV from both of the sets are shown in figure 6.3. Both of the samples have in-plane anisotropy as can be seen from the hysteresis loops. Clearly, the magnetic properties of the samples depend on the deposition conditions of the bottom Pt layer as the saturation field differs between the sample from set A and set B.

Also, the spectral dependence of polar magneto-optical Kerr effect varies between the samples from different sets which can be seen in figure 6.4.

X-ray reflectivity (XRR) measurements performed at the University of Bialystok and summed up in table 6.1 gave information about layer thicknesses and roughnesses. The sample from set B (750 °C) on which XRR was measured was prepared in the same deposition round as the sample investigated in this work. This was not possible for the sample from set A (RT) investigated here. Therefore XRR was measured on a sample from a different deposition round but prepared under the same conditions.

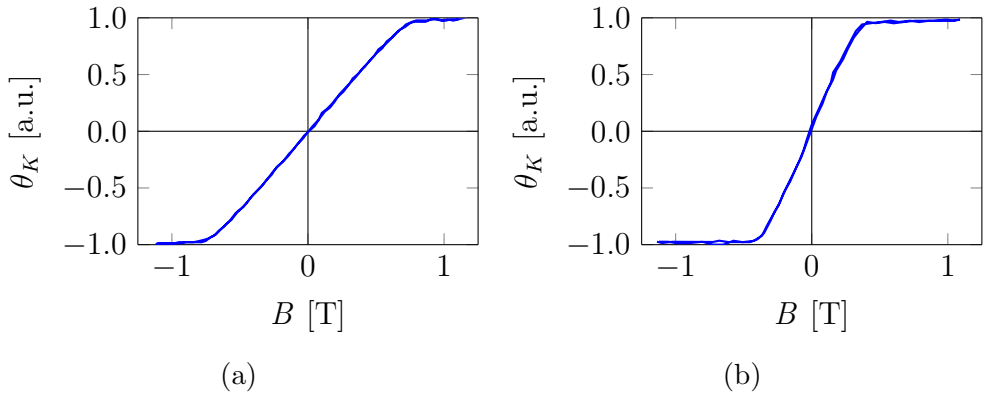

Figure 6.3: Polar Kerr rotation hysteresis loops at the photon energy 1.94 eV for non-irradiated Al_2O_3(0001)/Pt (5 nm)/Co (3.5 nm)/Pt (5 nm) samples from the set: (a) RT, (b) 750 °C. These measurements were performed at the University of Bialystok, Poland.

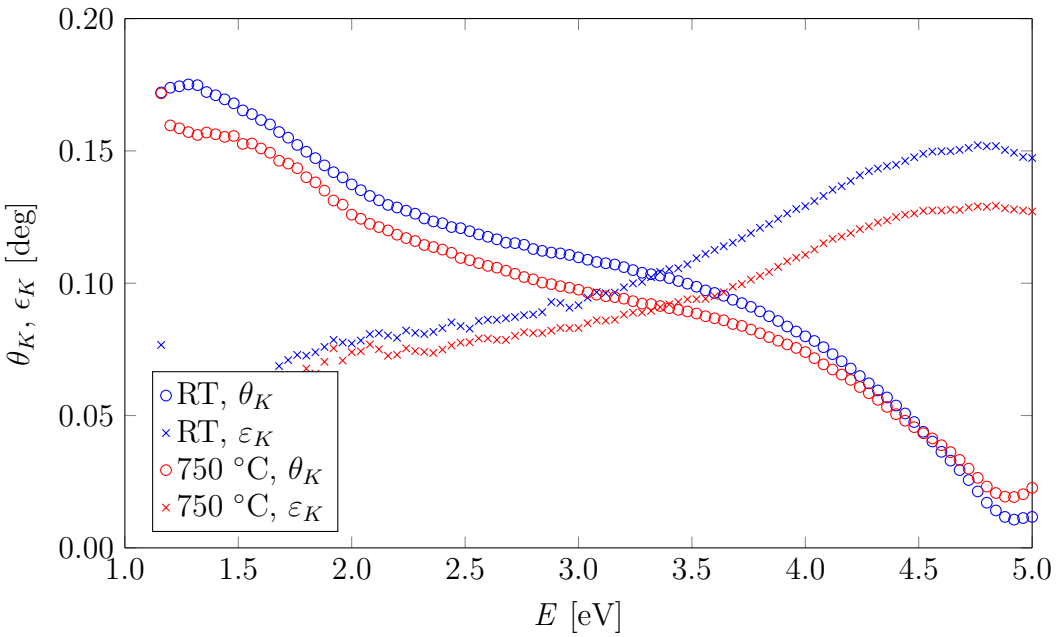

Figure 6.4: Comparison of polar Kerr rotation and ellipticity spectra of non-irradiated Al_2O_3(0001)/Pt (5 nm)/Co (3.5 nm)/Pt (5 nm) samples grown under different conditions.

Table 6.1: The thicknesses and roughnesses of individual layers fitted to XRR data measured at the University of Bialystok.

	Set A (RT)		Set B (750 °C)	
	Thickness [nm]	Roughness [nm]	Thickness [nm]	Roughness [nm]
Pt	4.80	0.69	4.61	0.84
Co	3.03	0.68	3.25	0.55
Pt	4.86	0.59	4.63	0.28
Al_2O_3	-	-	-	-

In order to calculate the off-diagonal elements of the permittivity tensor of the Co layer for each of the sample sets the knowledge of the diagonal elements of the permittivity tensor is needed. Spectroscopic ellipsometry was measured on the non-irradiated samples for the following angles of incidence: 55 deg, 60 deg and 65 deg. Layer thicknesses for the fitting of the results were taken from table 6.1. The roughness of the layers was described by effective medium approximation (EMA). The B-spline routine [59] was used to fit the optical constants of the Co layers. The optical constants of the substrate were taken from figure 6.2.

Figures 6.5 and 6.6 show the fitted optical constants of Co in the non-irradiated sample from set A (RT) and set B (750 °C) respectively. The optical constants are similar for both of the sets. Just for lower photon energies, there are subtle differences in the shape of the spectra. That might be caused by a difference in the carrier concentration or mobility.

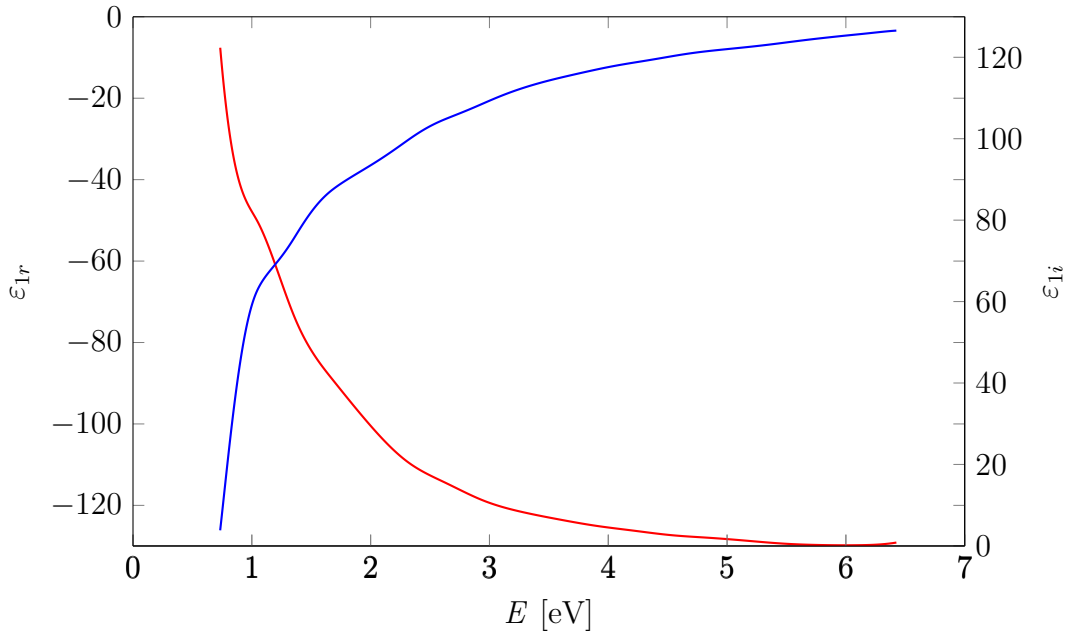

Figure 6.5: Real (blue line) and imaginary (red line) part of the diagonal elements of the tensor of permittivity of Co in the non-irradiated sample from set A (RT).

Using the optical constants of annealed Al_2O_3 shown in figure 6.2, the results of XRR fits in table 6.1 and the optical constants of Co in figures 6.5 and 6.6 the off-diagonal elements of the permittivity tensor of Co were calculated from the measured PMOKE spectra shown in figure 6.4. The optical constants of Pt were

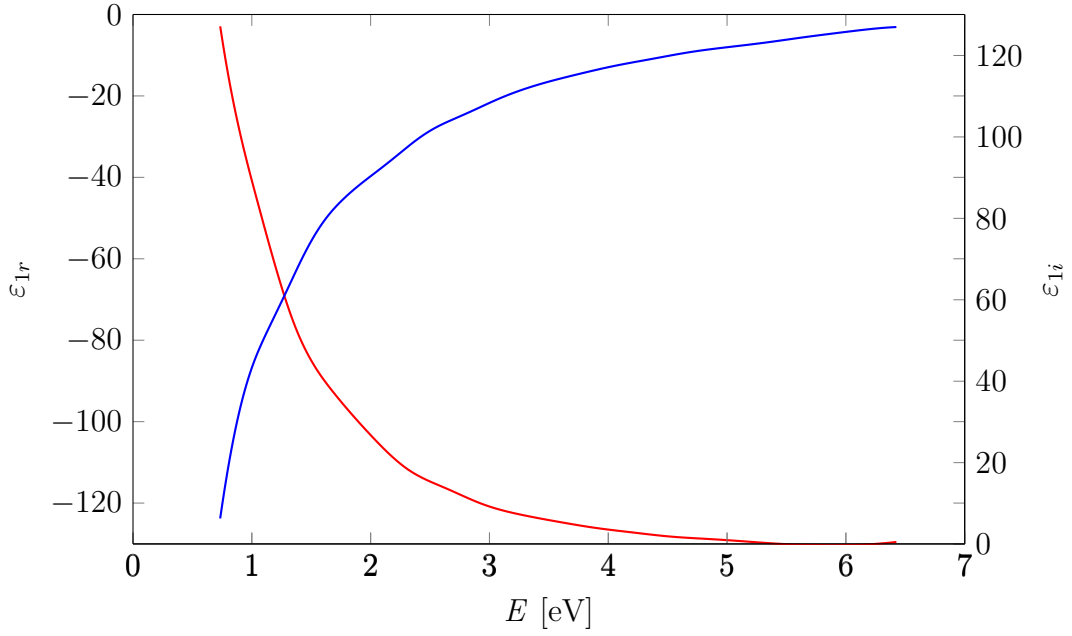

Figure 6.6: Real (blue line) and imaginary (red line) part of the diagonal elements of the tensor of permittivity of Co in the non-irradiated sample from set B (750 °C).

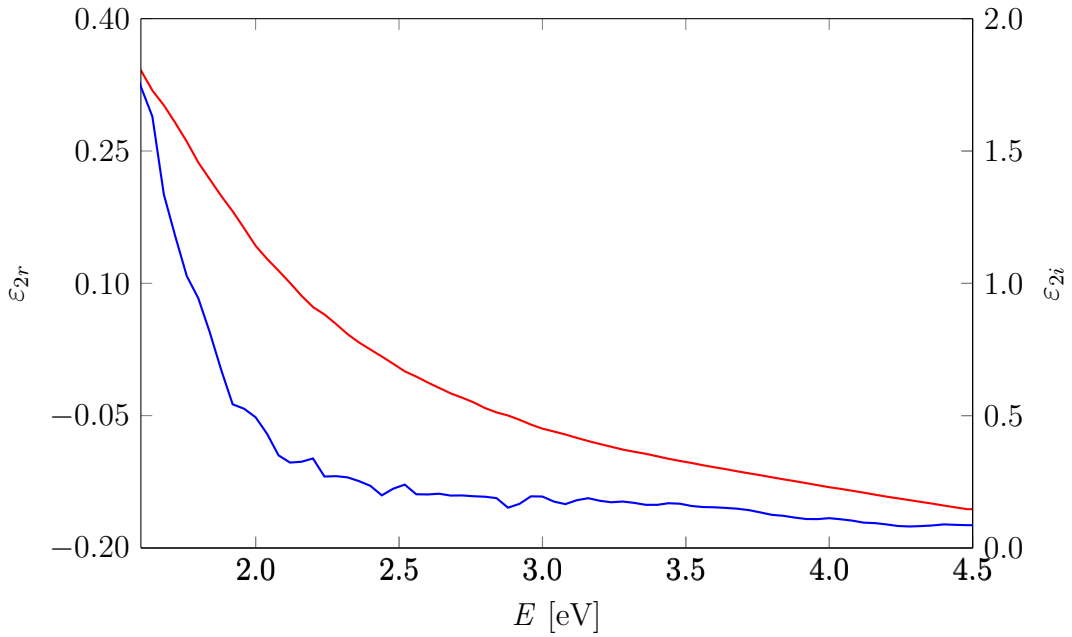

Figure 6.7: Real (blue line) and imaginary (red line) part of the off-diagonal elements of the tensor of permittivity of Co in the non-irradiated sample from set A (RT).

taken from Ref. [60]. Again the calculation was done separately for each sample set.

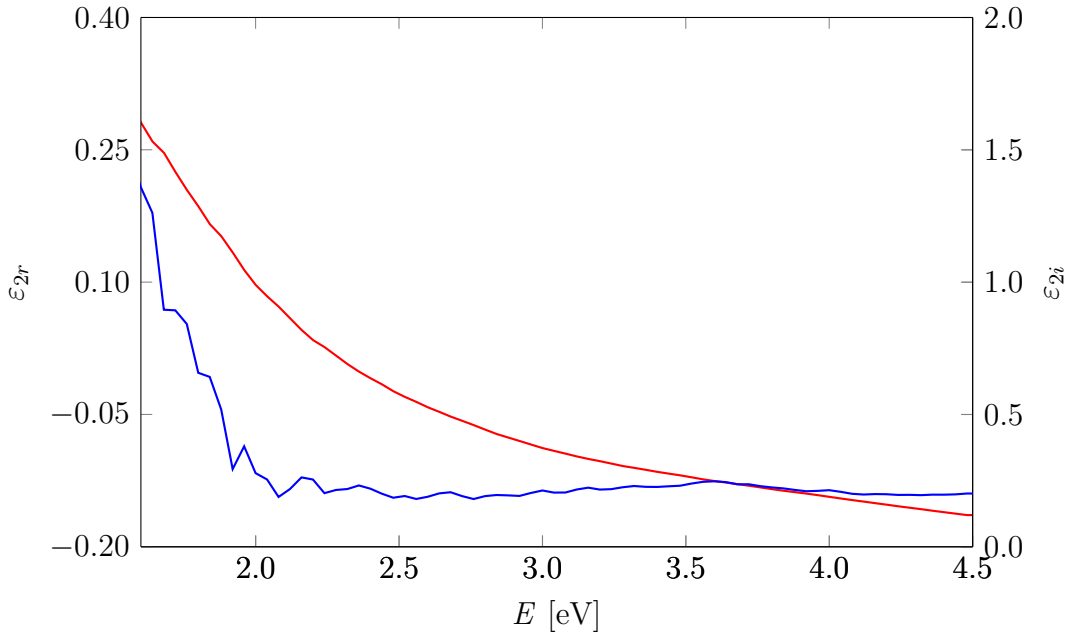

Figure 6.8: Real (blue line) and imaginary (red line) part of the off-diagonal elements of the tensor of permittivity of Co in the non-irradiated sample from set B (750 °C).

The spectral range in which the magneto-optical constants were calculated is limited by the spectral region in which the constants of the other materials present in the structures are known.

Figure 6.7 shows the calculted magneto-optical constants of Co in nanostructures from set A (RT). The constants of Co in samples from set B (750 °C) are shown in figure 6.8.

The amplitude of the magneto-optical constants is higher for the samples from set A (RT). The calculated ε_{2r} is noisy for both sets. In the case of set A (RT) ε_{2r} decreases monotonously with increasing photon energy. However, for the second set, ε_{2r} decreases at first but then starts to increase. The imaginary part of the off-diagonal element of the permittivity tensor has the same shape for both sets.

6.2.2 Irradiated samples

Each sample was irradiated by a single pulse of soft X-rays as described in chapter 5. Investigated samples from set A (RT) were irradiated by energy densities 15 mJ/cm^2 and 54 mJ/cm^2. Samples from set B (750 °C) were irradiated by energy densities 15 mJ/cm^2, 23 mJ/cm^2, 28 mJ/cm^2 and 54 mJ/cm^2.

Polar Kerr rotation hysteresis loops measured on the irradiated samples from set A are shown in figure 6.9. Both of the hysteresis loops are modified in comparison with the loop in figure 6.3a. For both of the modified samples, the saturation magnetic field is reduced. For the sample modified with the energy density 54 mJ/cm^2 a change in magnetic anisotropy also appears as the sample has non-zero

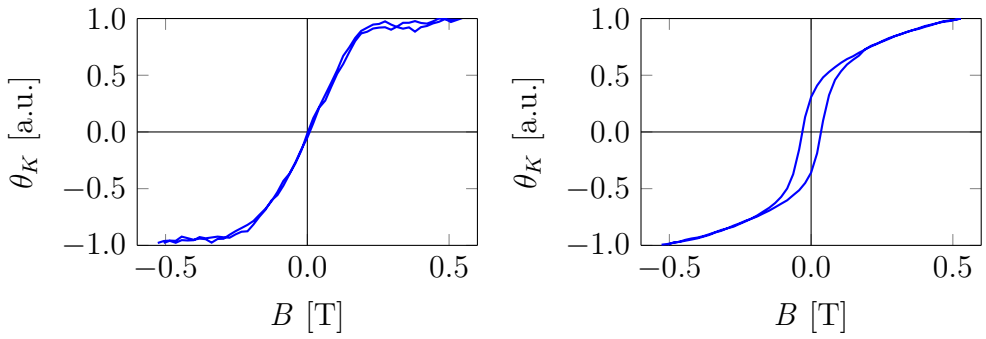

Figure 6.9: Polar Kerr rotation hysteresis loops at the photon energy 1.94 eV for Al_2O_3(0001)/Pt (5 nm)/Co (3.5 nm)/Pt (5 nm) samples from set A (RT) irradiated with a single pulse of energy density: (a) 15 mJ/cm^2, (b) 54 mJ/cm^2. These measurements were performed at the University of Bialystok, Poland.

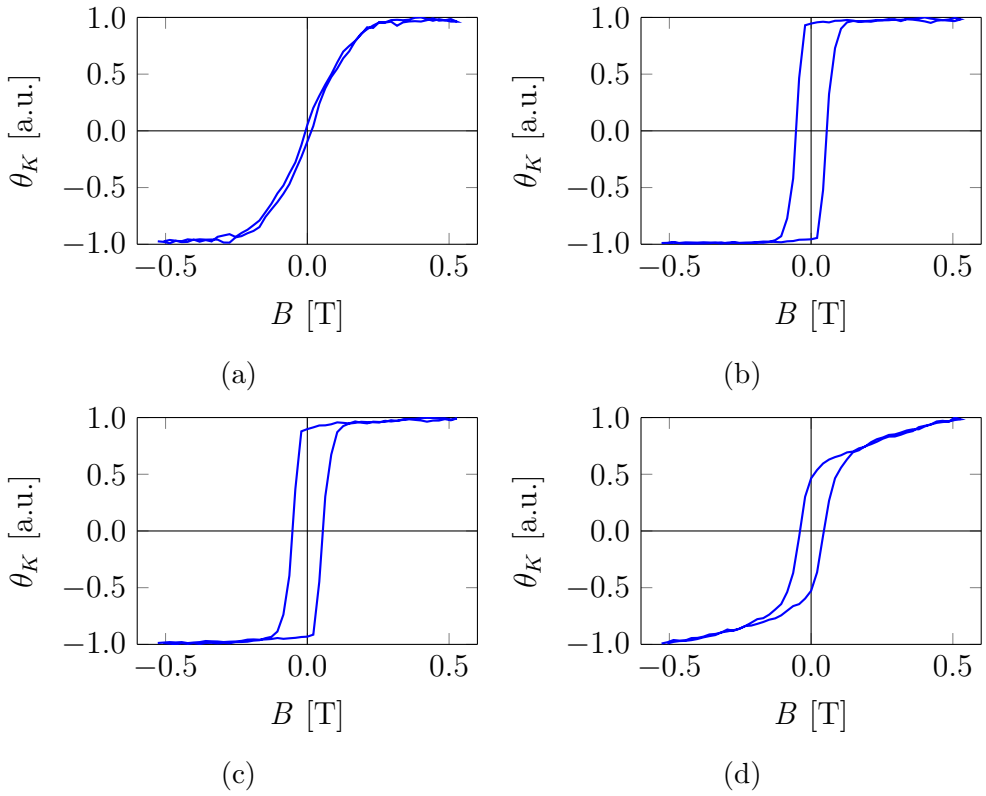

Figure 6.10: Polar Kerr rotation hysteresis loops at the photon energy 1.94 eV for Al_2O_3(0001)/Pt (5 nm)/Co (3.5 nm)/Pt (5 nm) samples from set B (750 °C) irradiated with a single pulse of energy density: (a) 15 mJ/cm^2, (b) 23 mJ/cm^2, (c) 28 mJ/cm^2, (d) 54 mJ/cm^2. These measurements were performed at the University of Bialystok, Poland.

magnetization in the out-of-plane direction in zero external magnetic field after irradiation.

Similar hysteresis loops for the irradiated samples from set B are presented in figure 6.10. Again, the hysteresis loops changed with irradiation for all of the energy densities used for modification.

The hysteresis loop of the sample irradiated with the energy density 15 mJ/cm^2 shown in figure 6.10a looks identical to the loop of the sample from set A irradiated by the same energy density even though the hysteresis loops of the non-irradiated samples differ.

The hysteresis loops of samples irradiated with energy densities 23 mJ/cm^2 and 28 mJ/cm^2 are very similar. PMA is induced for these energy densities.

After irradiation with the energy density 54 mJ/cm^2 magnetic anisotropy is changed but full PMA is not created as can be seen from the loop in figure 6.10d. The remanent magnetization is greater in this case than for the sample from set A irradiated by the same energy density.

Magneto-optical spectroscopy was measured on magnetically saturated samples for a nearly normal incidence of light.

The experimental spectra were compared to a theoretical calculation using 4×4 transfer matrix formalism. The permittivity tensors of the materials present in the structure and the layer thicknesses were the input of the theoretical calculations.

Previous work done on similar samples which is summed up in section 1.3.2 has shown that CoPt alloys are created upon irradiation. To include them in the theoretical calculations the knowledge of their optical and magneto-optical constants is necessary.

The diagonal elements of the tensor of permittivity of CoPt alloys were calculated by EMA. The off-diagonal elements were then calculated from magneto-optical spectra reported by Brandle et al and Visnovsky et al [61, 62].

The spectral dependences of ε_1 and ε_2 calculated in section 6.2.1 were used as constants of pure Co (not in alloys) in the samples.

The dependence of the concentration of Co on the depth was approximated by a stepwise profile with these Co concentrations: 0 %, 28 %, 47 %, 59 %, 72 % and 100 %.

Thicknesses of individual layers in the theoretical calculation were modified until the best agreement between the measured spectra and the theoretical calculation was achieved. These thicknesses then give the profiles of the samples.

PMOKE spectra measured on irradiated samples from set A and theoretical models are shown in figure 6.11. The parameters of the models are summarized in table 6.2. Spectra of Kerr rotation in figure 6.11a are compared to theoretical calculations of θ_K in figure 6.11b. Similarly, the measured spectra of Kerr ellipticity are in figure 6.11c and the calculated ones in figure 6.11d. A calculation for a nanostructure with nominal layer thicknesses from table 6.1 is included as well.

The theoretical modeling which assumes intermixing of adjacent layers and the formation of CoPt alloys manages to describe the trend of the observed changes in PMOKE spectra very well.

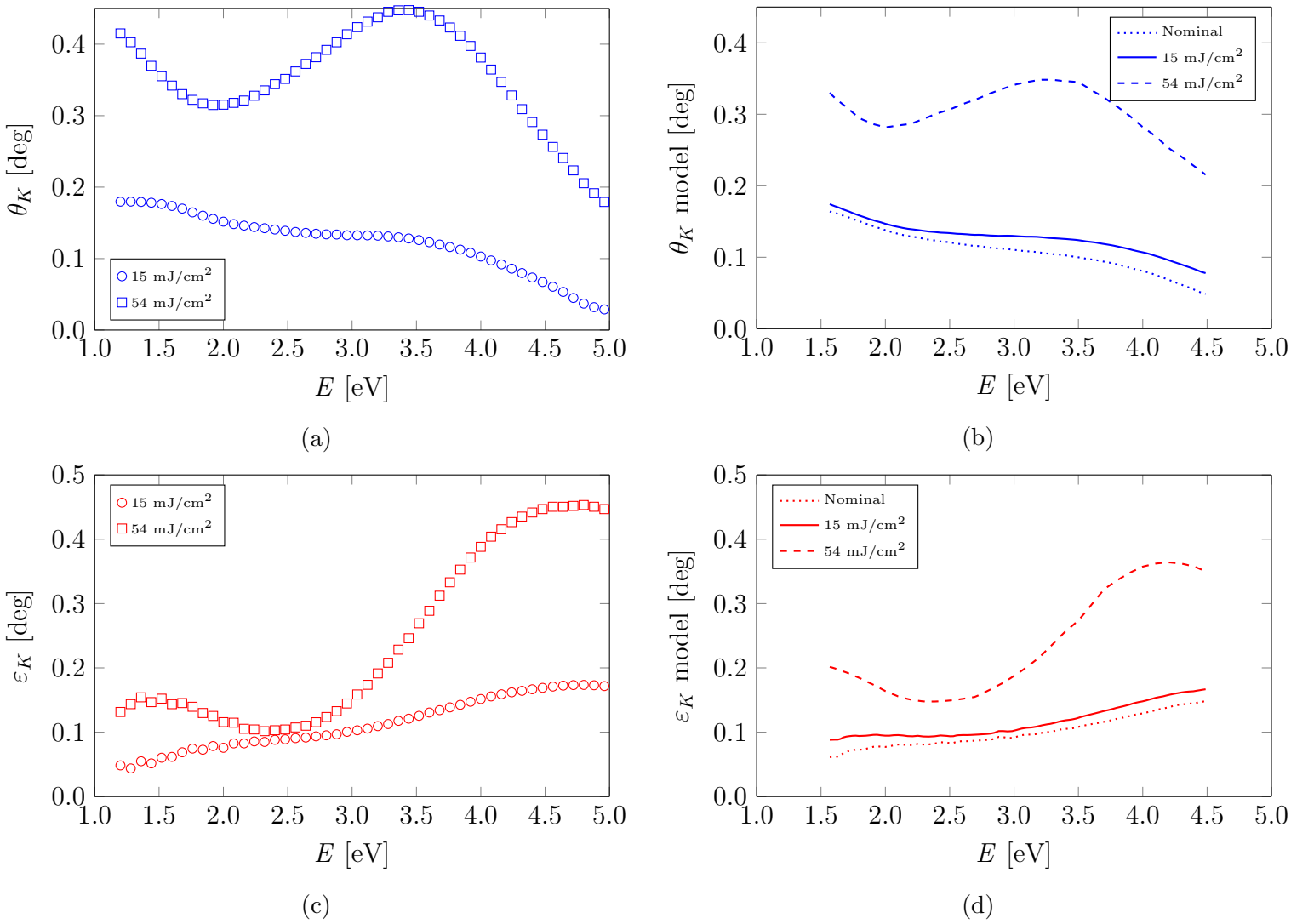

Figure 6.11: Polar Kerr rotation and ellipticity spectra of Al_2O_3(0001)/Pt (5 nm)/Co (3.5 nm)/Pt (5 nm) from set A (RT) irradiated by 15 mJ/cm^2 and 54 mJ/cm^2 and the theoretical models. A theoretical calculation for the nominal layer thicknesses (taken from table 6.1) is included in the graphs for comparison.

The agreement between the experimental and the measured spectral dependence of PMOKE for the sample irradiated with the energy density 15 mJ/cm^2 is good. The only difference is for the ellipticity in the infrared region.

Irradiation by energy density 54 mJ/cm^2 results in a significant modification of PMOKE. The amplitude is increased and the modulation of Kerr rotation around the energy of 2 eV gets more pronounced. Both of these can be attributed to the creation of CoPt alloys. The nanostructures are totally intermixed and some material is evaporated from the sample according to the models. The spectral shape of the calculation agrees well with the experimental data. However, the amplitude is different.

Table 6.2: Layer thicknesses for which the best agreement between the measured PMOKE spectra and the theoretical calculations was achieved for sample set A (RT).

	15 mJ/cm^2	54 mJ/cm^2
	Layer thickness [nm]	Layer thickness [nm]
Pt	4.64	0
$Co_{0.28}Pt_{0.72}$	0	0
$Co_{0.47}Pt_{0.53}$	0.6	0
$Co_{0.59}Pt_{0.41}$	0.3	0
$Co_{0.72}Pt_{0.28}$	0.2	0
Co	2.46	0
$Co_{0.72}Pt_{0.28}$	0.2	0
$Co_{0.59}Pt_{0.41}$	0.3	0
$Co_{0.47}Pt_{0.53}$	0.6	0
$Co_{0.28}Pt_{0.72}$	0	9
Pt	4.66	1
Al_2O_3	-	-

The results of PMOKE spectroscopy and theoretical calculations for set B (750 °C) are in figure 6.12. The layer thicknesses used in the models are listed in table 6.3.

For the sample irradiated by 15 mJ/cm^2, the theoretical models do not indicate any intermixing unlike for the sample from the other set irradiated by the same energy density. The PMOKE spectra of this sample are nearly identical to the non-irradiated sample. The only differences are for the lower photon energies where the amplitude is reduced compared to the non-irradiated sample. This reduction is hard to describe within our model because alloying and potential evaporation of Pt from the top layer both increase the amplitude. The explanation might be the effect of strain. Because the nanostructures from sets A and B were grown under different conditions the strain in them may vary. The initial difference in strain may influence the way the samples respond to irradiation.

The layer thicknesses for the sample irradiated by 15 mJ/cm^2 listed in table 6.3 correspond to the layer thicknesses of the non-irradiated sample determined by XRR (shown in table 6.1). That is also the reason why the model for the nominal structure is not shown for this set - it overlaps with the model for the sample irradiated by 15 mJ/cm^2. The roughness was neglected as it did not significantly influence the results.

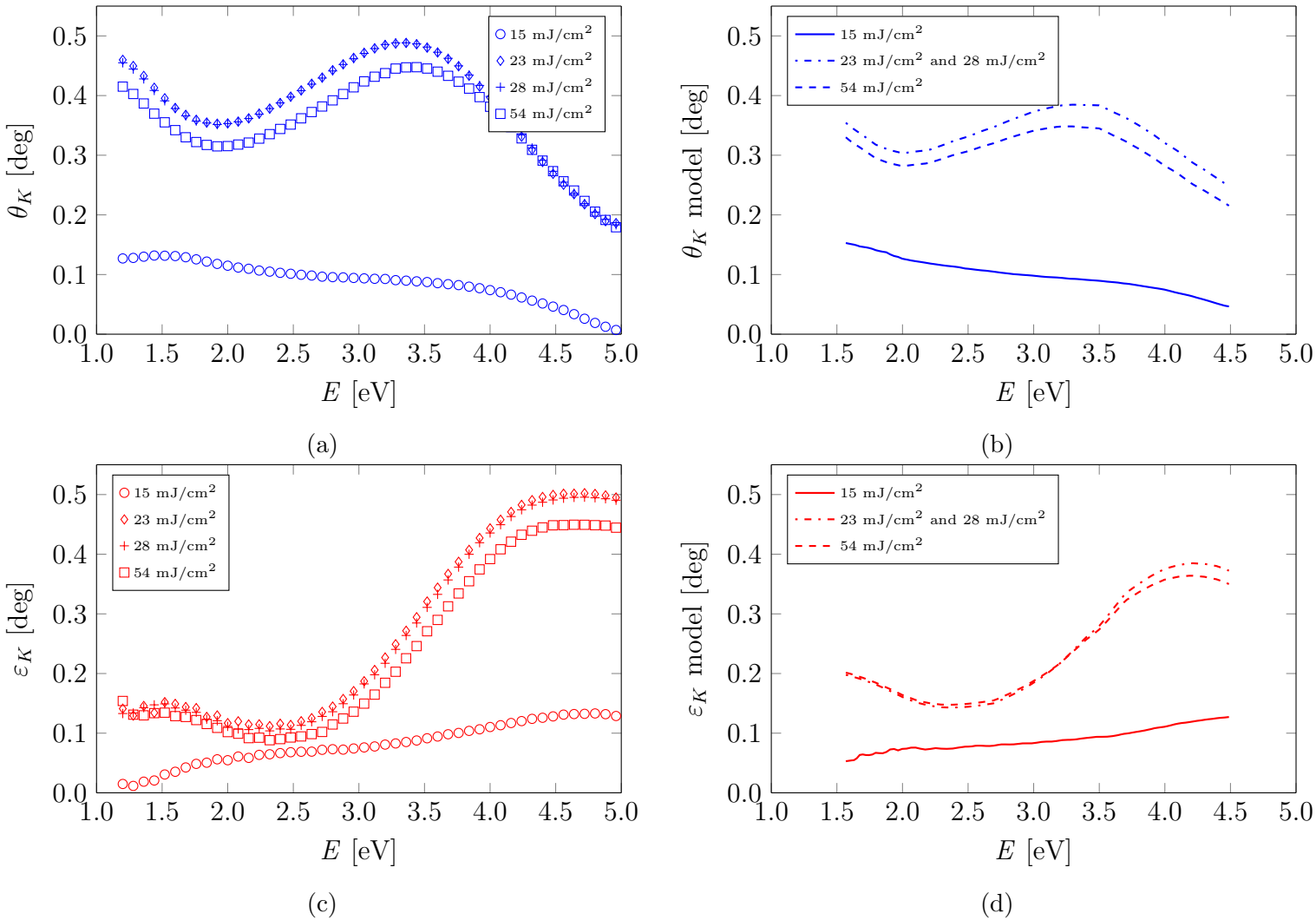

Figure 6.12: Polar Kerr rotation and ellipticity spectra of Al_2O_3(0001)/Pt (5 nm)/Co (3.5 nm)/Pt (5 nm) from set B (750 °C) irradiated by various energy densities and the theoretical models.

A big modification of PMOKE spectra is visible after irradiation by 23 mJ/cm^2, 28 mJ/cm^2 and 54 mJ/cm^2.

The spectra of the samples irradiated by 23 mJ/cm^2 and 28 mJ/cm^2 are very similar as are their hysteresis loops (figures 6.10b and 6.10c). Modeling suggests that the Pt and Co layers get totally intermixed (parameters are in table 6.3). In contrast to the sample from set A irradiated by 54 mJ/cm^2, less material is removed from the sample. The theoretical calculation does not manage to describe the amplitude of the measured spectra fully.

The amplitude of PMOKE spectra measured on the sample irradiated by a pulse of energy density 54 mJ/cm^2 is lower than for samples irradiated with 23 mJ/cm^2 and 28 mJ/cm^2. It is difficult to ascribe this to a single cause. One possibility is that some Co atoms are removed from the structure by irradiation. However, that does not always lead to a decrease in amplitude of both Kerr rotation and ellipticity because the trilayers are very thin and removal of some material from the sample increases the contribution of the substrate.

Another point which needs to be taken into account is the thickness of the bottom Pt layer. For the samples irradiated with energy densities of 23 mJ/cm^2 and 28 mJ/cm^2 the layers get totally intermixed. However, it is important to realize that unlike in the case of ion irradiation studied further in this chapter laser irradiation does not have to cause gradual changes. When the X-ray pulse is absorbed by the sample non-equilibrium thermodynamical processes occur. In the case of lower energies, the temperature of the lattice might be increased and the layers totally intermix and for higher energies, a part of the sample might be evaporated and the rest does not intermix totally.

The theoretical calculations give the best agreement for the layer thicknesses specified in table 6.3. Therefore we suggest that a fraction of the Co and Pt atoms is removed from the sample and a 1 nm thick Pt layer remains between the intermixed layer and the substrate. However, the system and the analysis is complicated and more measurements are necessary to confirm this.

In summary, strong modifications of the spectral dependence of PMOKE are visible for samples irradiated with a pulse of soft X-rays. This indicates the creation of Pt-rich CoPt alloys. The theoretical calculations describe the trends of the changes of the PMOKE spectra well. The disagreement in the experimental and calculated PMOKE amplitudes of the samples irradiated with higher energy densities may be caused by a presence of different CoPt alloys than the ones used in the models as the analysis in this work was restricted by the CoPt alloy constants available.

The CoPt alloy which provided the best agreement between the experimental data and the calculations for higher irradiating energies has a ratio of Co and Pt close to the ratio in the disordered $CoPt_3$ alloy with magnetic anisotropy [41]. The creation of this alloy might be responsible for the observed changes in magnetic properties.

The effect of strain and the potential modification of the substrate by the X-rays also have to be considered when interpreting the magneto-optical spectra.

Table 6.3: Layer thicknesses for which the best agreement between the measured PMOKE spectra and the theoretical calculations was achieved for sample set B (750 °C).

	15 mJ/cm^2	23 mJ/cm^2	28 mJ/cm^2	54 mJ/cm^2
	Layer thickness [nm]	Layer thickness [nm]	Layer thickness [nm]	Layer thickness [nm]
Pt	4.89	0	0	0
$Co_{0.28}Pt_{0.72}$	0	0	0	0
$Co_{0.47}Pt_{0.53}$	0	0	0	0
$Co_{0.59}Pt_{0.41}$	0	0	0	0
$Co_{0.72}Pt_{0.28}$	0	0	0	0
Co	3.67	0	0	0
$Co_{0.72}Pt_{0.28}$	0	0	0	0
$Co_{0.59}Pt_{0.41}$	0	0	0	0
$Co_{0.47}Pt_{0.53}$	0	0	0	0
$Co_{0.28}Pt_{0.72}$	0	12	12	9
Pt	4.77	0	0	1
Al_2O_3	-	-	-	-

6.3 Modification by Ga^+ ions

6.3.1 Al_2O_3/Pt/Co/Pt

Polar Kerr microscopy remanence image taken of the irradiated Al_2O_3/Pt/Co/Pt sample is shown in figure 6.13. From this image it is visible that the non-irradiated stripe (bottom of the image) has in-plane magnetic anisotropy. Certain ion fluences result in enhanced PMA. Two branches of enhanced PMA are observed in accordance with the previously reported results which were summarized in section 1.3.1.

PMOKE spectroscopy was measured on all of the irradiated stripes in high enough magnetic field to saturate the sample. Measurements were performed with p-polarized light and at the 64.5 degrees angle of incidence. Due to the irradiated stripes being narrow focusing optics was needed. The proximity of the lenses to the magnet resulted in parasitic Faraday rotation in the material of the lenses. In order to subtract this parasitic contribution from the measured PMOKE spectra, a Ru sample was measured as well. This material exhibits zero Kerr effect, therefore the spectra measured on this sample correspond to the contribution of the optics elements near the magnet.

The photon energy of 4.52 eV was chosen to demonstrate the dependence of the amplitude of Kerr rotation on the ion dose used to irradiate the stripe. The graph is shown in figure 6.14.

The observed evolution of the Kerr rotation amplitude with ion dose may be explained by three main contributions. First of all, the intermixing of the Co and Pt layers increases the amplitude of Kerr rotation as CoPt alloys have a higher amplitude at this wavelength than pure Co.

Secondly, etching of the top Pt layer also increases the amplitude as the frac-

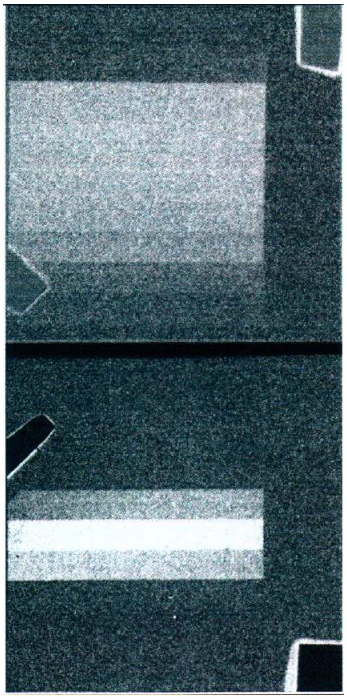

Figure 6.13: A polar Kerr microscopy remanence image of the Al_2O_3/Pt/Co/Pt sample irradiated in stripes with increasing ion fluence from bottom up. These measurements were performed at the University of Bialystok, Poland.

tion of the magnetic material in the sample grows with this.

Finally, as the intermixing gets more significant with higher ion fluences the Co atoms get closer to the surface of the samples. Etching depth also increases with ion dose. Therefore for high ion fluences, Co atoms are removed from the sample as well which results in a decrease of the measured Kerr rotation amplitude.

Figure 6.14 can be interpreted in the following way: with ion irradiation the Kerr rotation amplitude increases because of the intermixing of adjacent layers and the resulting formation of CoPt alloys. As the number of bombarding ions increases the resulting etching rises. At first, only Pt is removed from the sample which further increases the Kerr rotation amplitude but for higher doses the Co atoms are etched away too which has the opposite effect.

Similarly as in section 6.2, the measured spectral dependencies for each stripe were compared to theoretical calculations in order to estimate the profile of the structures after irradiation and connect it to the observed magnetic properties. The optical constants of Co were taken from Ref. [60] and the magneto-optical ones from Ref. [62].

The results of modeling of four stripes are presented here - the non-irradiated one and three irradiated ones. One irradiated stripe was chosen from branch 1 of the enhanced PMA (the brightest stripe in figure 6.13), one from between branch 1 and 2 and the last one from branch 2. Hysteresis loops for the selected stripes are shown in figure 6.15.

PMOKE spectra of these stripes and the theoretical models are shown in figure 6.16. The parameters of the theoretical models are listed in table 6.4.

The first thing to notice is that the PMOKE spectra of the non-irradiated samples are very different to the spectra of the reference samples from the sets

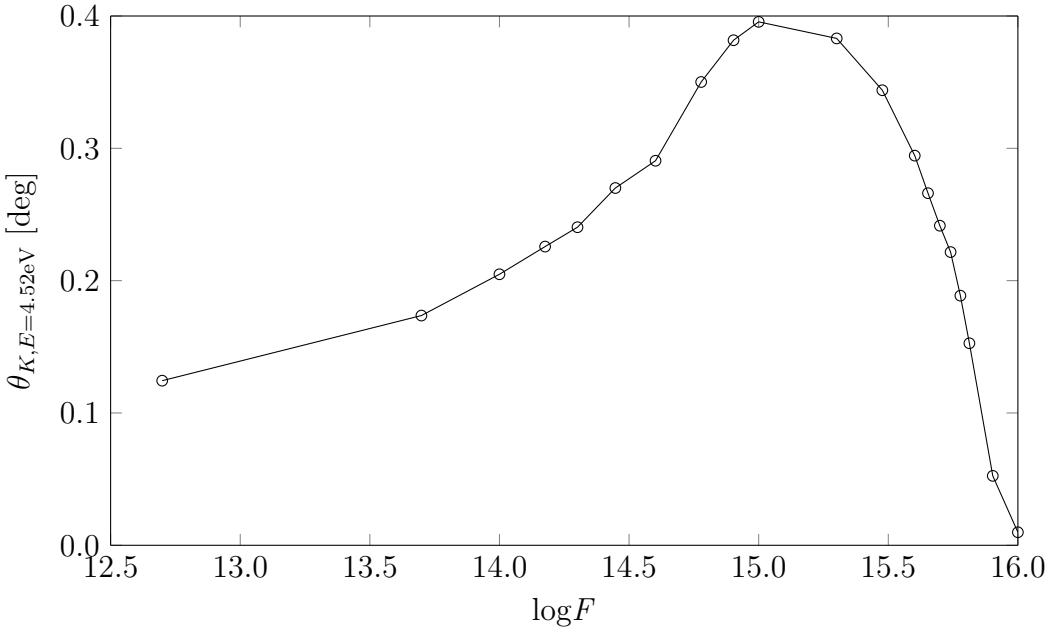

Figure 6.14: Polar Kerr rotation amplitude at the photon energy of 4.52 eV as a function of Ga^+ ion fluence F in ions/cm^2 measured on Al_2O_3/Pt/Co/Pt nanostructures.

irradiated by soft X-rays (figure 6.4). This is caused by the different thickness of the Pt buffer which influences how much light gets to and therefore "experiences" the substrate and also by the different angle of incidence between the measurements of the samples irradiated by a laser and by ions. The difference in the Co layer thickness also plays a role.

The models suggest that the layers are already partly intermixed for the as-grown sample (let us point out that the XRR measurements used in section 6.2 were not capable of distinguishing roughness and intermixing). The agreement between the models and the experiment is not ideal for the non-irradiated sample. The theoretical calculations describe the spectral dependence of Kerr rotation rather well but the calculated spectrum of ellipticity has a similar shape but is shifted. The situation improves a little when the constants calculated in section 6.2 are used but not much (not shown here). That is interesting but as shown in section 6.2 the properties of the nanostructures are very sensitive to the preparation technique. It is possible that in this case the difference in the thickness of the Co layer in this sample and the non-irradiated samples from section 6.2 also influences the properties.

XRR measurements of the non-irradiated sample were not possible in this case as the sample was inhomogeneous (it consisted of many stripes irradiated with different ion fluences).

According to the model, the intermixing is significant and there is nearly no pure Co left in the stripe irradiated by 2×10^{14} ions/cm^2. That indicates that the disagreement in ellipticity between the measurement and the model in the case of the non-irradiated sample might be caused by the constants of Co used in the calculation because the models fit much better once there is next to no pure Co in the nanostructures. The etching of the top Pt layer is negligible.

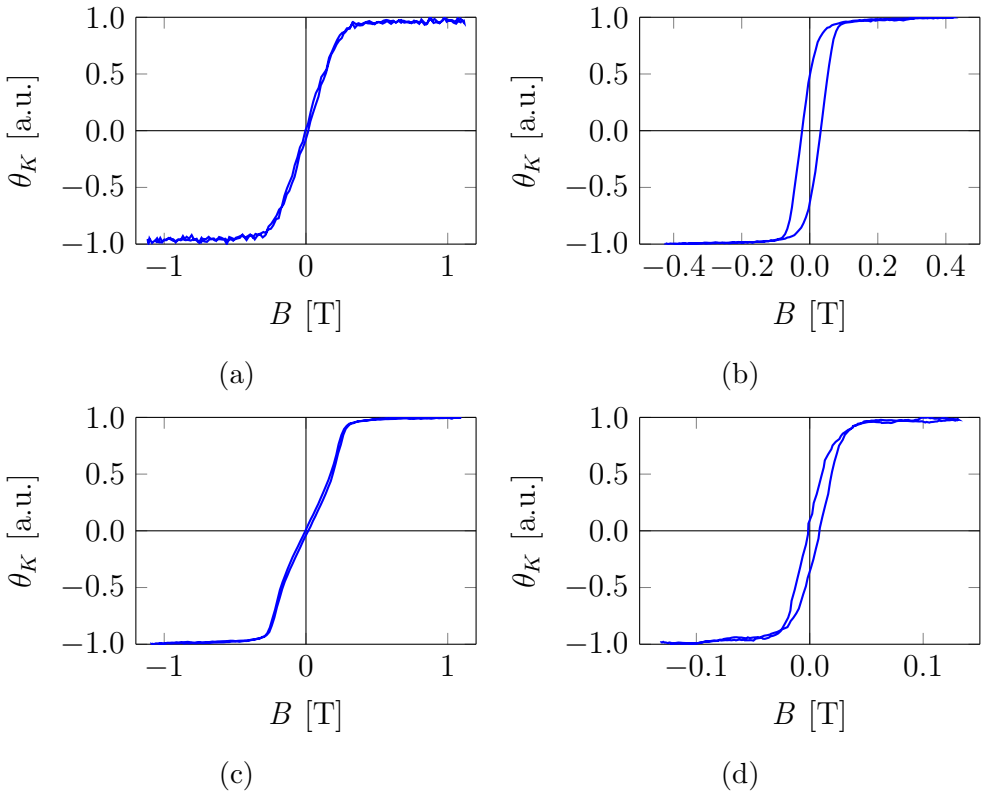

Figure 6.15: Polar Kerr rotation hysteresis loops at the photon energy 1.94 eV for a stripe of the Al_2O_3(0001)/Pt/Co/Pt nanostructure irradiated by the following ion dose: (a) 0 ions/cm^2, (b) 2×10^{14} ions/cm^2, (c) 6×10^{14} ions/cm^2, (d) 5×10^{15} ions/cm^2. These measurements were performed at the University of Bialystok, Poland.

Table 6.4: Layer thicknesses for which the best agreement between the measured PMOKE spectra and the theoretical calculations was achieved for the Al_2O_3/Pt/Co/Pt sample set irradiated with ions.

	0 ions/cm^2	2×10^{14} ions/cm^2	6×10^{14} ions/cm^2	5×10^{15} ions/cm^2
	Layer thickness [nm]	Layer thickness [nm]	Layer thickness [nm]	Layer thickness [nm]
Pt	4.8	3.05	1.6	0
$Co_{0.28}Pt_{0.72}$	0.15	1.7	3	0
$Co_{0.47}Pt_{0.53}$	0.1	0.95	1.4	0
$Co_{0.59}Pt_{0.41}$	0.05	0.4	0	0
$Co_{0.72}Pt_{0.28}$	0.05	0.2	0	0
Co	2.69	0.39	0	0
$Co_{0.72}Pt_{0.28}$	0.05	0.2	0	0
$Co_{0.59}Pt_{0.41}$	0.05	0.4	0	0
$Co_{0.47}Pt_{0.53}$	0.1	0.95	1.4	0
$Co_{0.28}Pt_{0.72}$	0.15	1.7	3	4.9
Pt	19.8	18.05	17.1	16.37
Al_2O_3	-	-	-	-

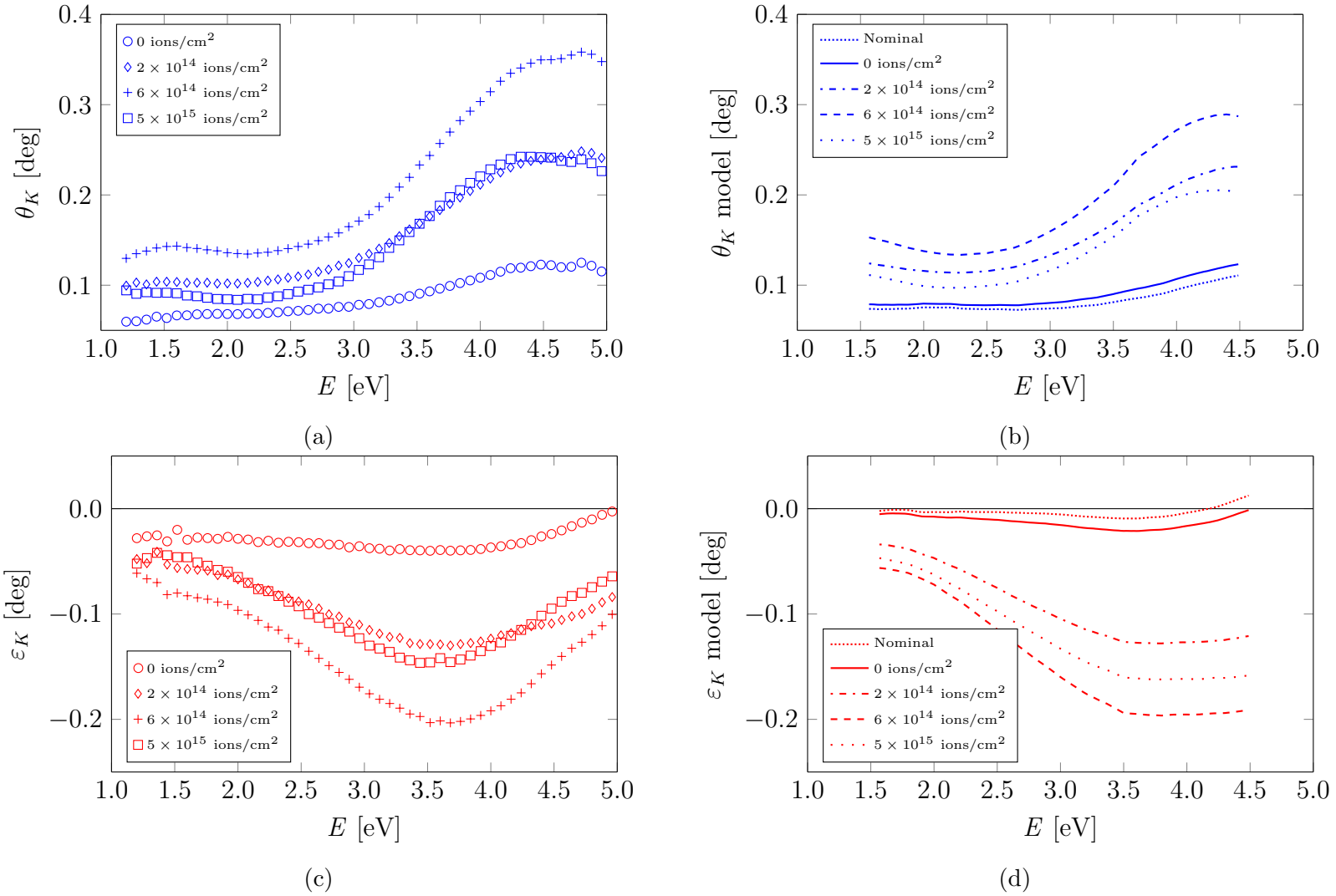

Figure 6.16: Polar Kerr rotation and ellipticity spectra of Al_2O_3(0001)/Pt (20 nm)/Co (3 nm)/Pt (5 nm) irradiated by various ion fluences and the theoretical models. A theoretical calculation for the nominal layer thicknesses is included in the graphs for comparison.

The stripe irradiated by 6×10^{14} ions/cm^2 does not exhibit enhanced PMA as can be seen from the hysteresis loop in figure 6.15c. The shape of the loop indicates the presence of two phases with different magnetic properties. The theoretical models indicate that no pure Co is present in this stripe and also the Co-rich alloys have disappeared. The etching is estimated to be around 0.5 nm.

The models suggest significant intermixing and etching for the sample irradiated by the ion fluence of 5×10^{15} ions/cm^2. Only the CoPt alloy with the highest percentage of Pt is present according to the calculations. Due to the high level of intermixing, it is reasonable to expect that alloys with an even higher concentration of Pt are present in the nanostructure. Unfortunately, that could not be included in the simulations due to the lack of their constants.

Generally, the theoretical calculations describe the trends in the PMOKE spectra with irradiation rather well. The measured spectral shape of ellipticity differs from the calculation for higher photon energies for samples irradiated by 6×10^{14} ions/cm^2 and 5×10^{15} ions/cm^2. The models also do not predict the crossing of the spectra for the samples irradiated by 2×10^{14} ions/cm^2 and 5×10^{15} ions/cm^2.

These disagreements might be caused by a creation of CoPt alloys with a different composition than the compositions of the alloys used in the calculations.

The models presented here calculate with equal intermixing at the top and the bottom interface. However, logically the intermixing at the top interface should be higher. It is questionable though how high the difference in the intermixing is and it might be negligible as the mean implantation depth is around 10 nm [19]. Unfortunately, the models are only sensitive to significant differences in top and bottom interface intermixing so they do not provide much information about the small differences in intermixing. These differences were therefore neglected.

6.3.2 Al_2O_3/Pt/Au/Co/Au

A polar Kerr rotation remanence image of the Al_2O_3/Pt/Au/Co/Au sample irradiated in stripes shown in figure 6.17 reveals that for no stripe there is any out-of-plane magnetization in zero outer magnetic field.

Polar Kerr magneto-optical spectroscopy was measured on each of the stripes. The results were corrected for the parasitic Faraday rotation caused by the stray field from the electromagnet.

The polar Kerr rotation amplitude is plotted as a function of ion dose in figure 6.18, this time for the photon energy of 3.72 eV.

For lower ion fluences, the amplitude decreases at first and then increases again but the changes are not big. Doses above $F = 2.8 \times 10^{14}$ ions/cm^2 result in a rapid drop of the amplitude. For the highest ion fluences, the amplitude is close to zero.

Co and Au are immiscible. Therefore, we can suppose that ion bombardment results in Co nanoparticles dispersing in Au. EMA can be used to estimate the optical a magneto-optical constants of such material [63]. We supposed spherical shape of the Co nanoparticles in the calculations.

Theoretical calculations predict that intermixing of the Co and Au layers decreases the amplitude of PMOKE. The effect is not strong though and significant intermixing is needed to see an effect on the calculated spectra.

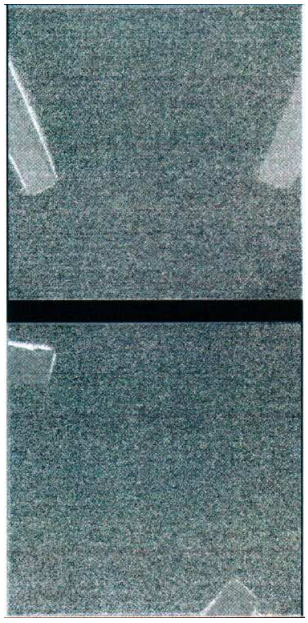

Figure 6.17: A polar Kerr microscopy remanence image of the Al_2O_3/Pt/Au/Co/Au sample irradiated in stripes with increasing ion fluence from bottom up. These measurements were performed at the University of Bialystok, Poland.

As in the case of Pt, etching of the top Au layer also increases PMOKE amplitude. For higher levels of irradiation, the Co atoms are removed from the sample as well which results in a drop of amplitude.

Bearing these effects in mind the graph in figure 6.18 may be interpreted followingly: the ion irradiation intermixes the Co and Au layers with minimal effects on the Kerr spectra. For higher ion doses the etching and intermixing is stronger resulting in a removal of Co atoms from the sample and the consequential decrease in the amplitude of the PMOKE spectra. The highest of the used ion fluences leave few magnetic atoms in the samples.

From the comparison of the ion dose for which the PMOKE amplitude drops for this sample and the Al_2O_3/Pt/Co/Pt sample and also the ion fluences resulting in close to zero amplitudes it is possible to say that Au is etched more easily than Pt by Ga^+ ions.

Results of measurements on stripes irradiated by the same fluences as for Al_2O_3/Pt/Co/Pt are presented here except for the highest fluence which corresponds to nearly zero amplitude for this sample.

The hysteresis loops measured on the selected stripes and shown in figure 6.19 confirm that no changes of magnetic anisotropy appear. Just for the fluence of 6×10^{14} ions/cm^2 the shape of the loop indicates a presence of different magnetic phases.

Magneto-optical measurements were compared to theoretical models. Both of these are shown in figure 6.20. Intermixing was included in the models by EMA of Co particles in Au matrix with four different percentages of Co in the material. All the parameters of models are listed in table 6.5.

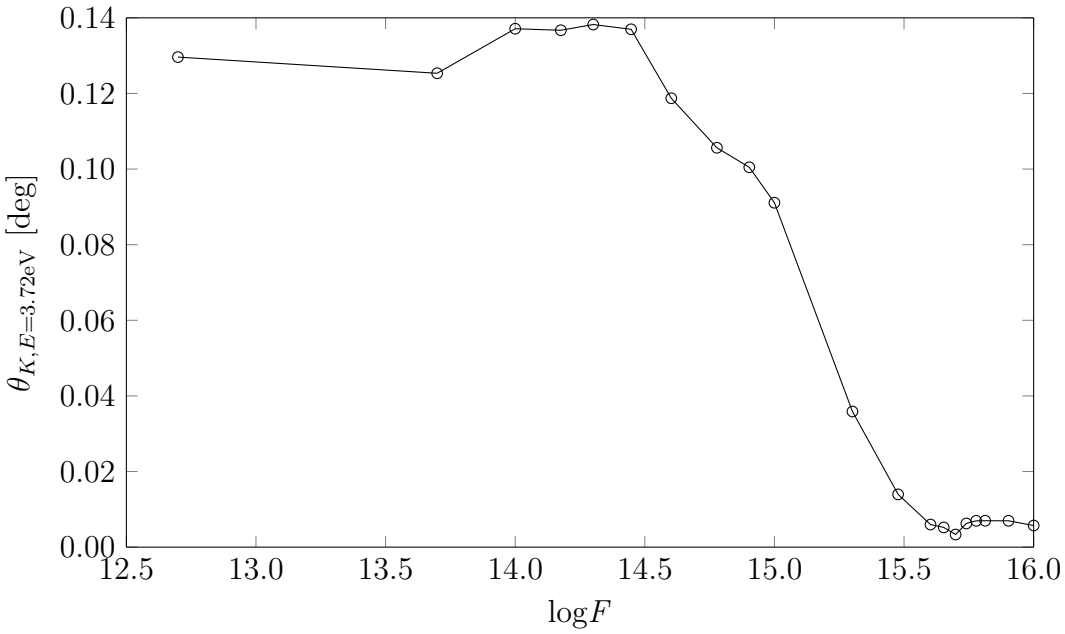

Figure 6.18: Polar Kerr rotation amplitude at the photon energy of 3.72 eV as a function of Ga^+ ion fluence F in ions/cm^2 measured on Al_2O_3/Pt/Au/Co/Au nanostructures.

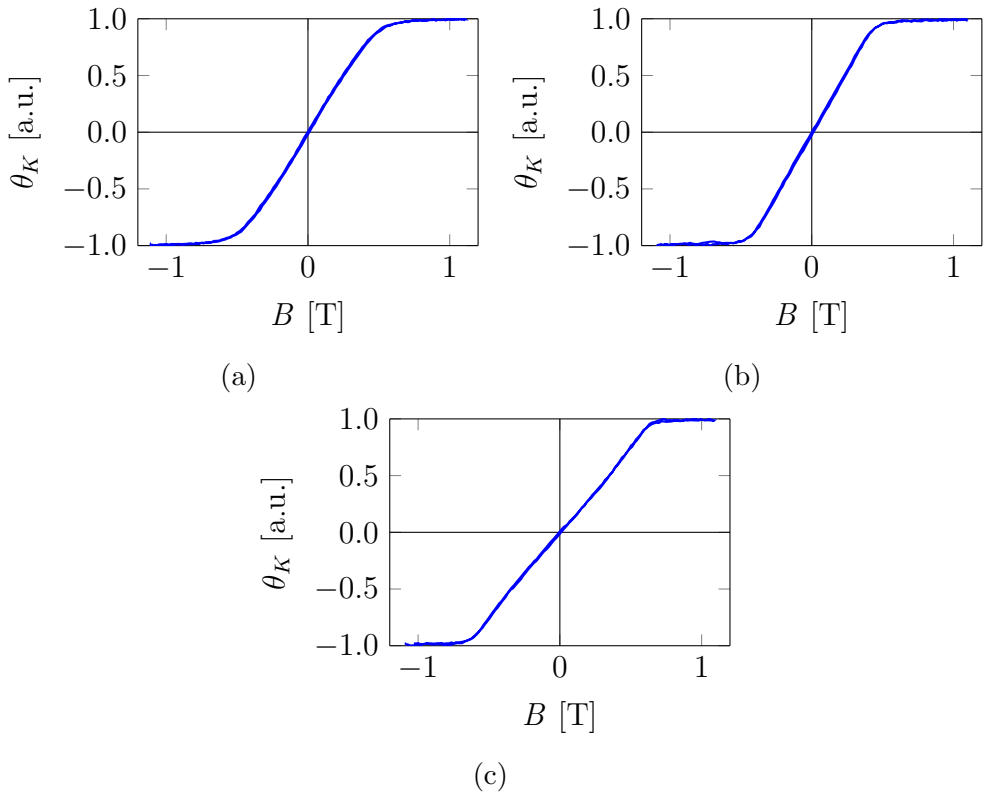

Figure 6.19: Polar Kerr rotation hysteresis loops at the photon energy 1.94 eV for a stripe of the Al_2O_3/Pt/Au/Co/Au nanostructure irradiated by the following ion dose: (a) 0 ions/cm^2, (b) 2×10^{14} ions/cm^2, (c) 6×10^{14} ions/cm^2. These measurements were performed at the University of Bialystok, Poland.

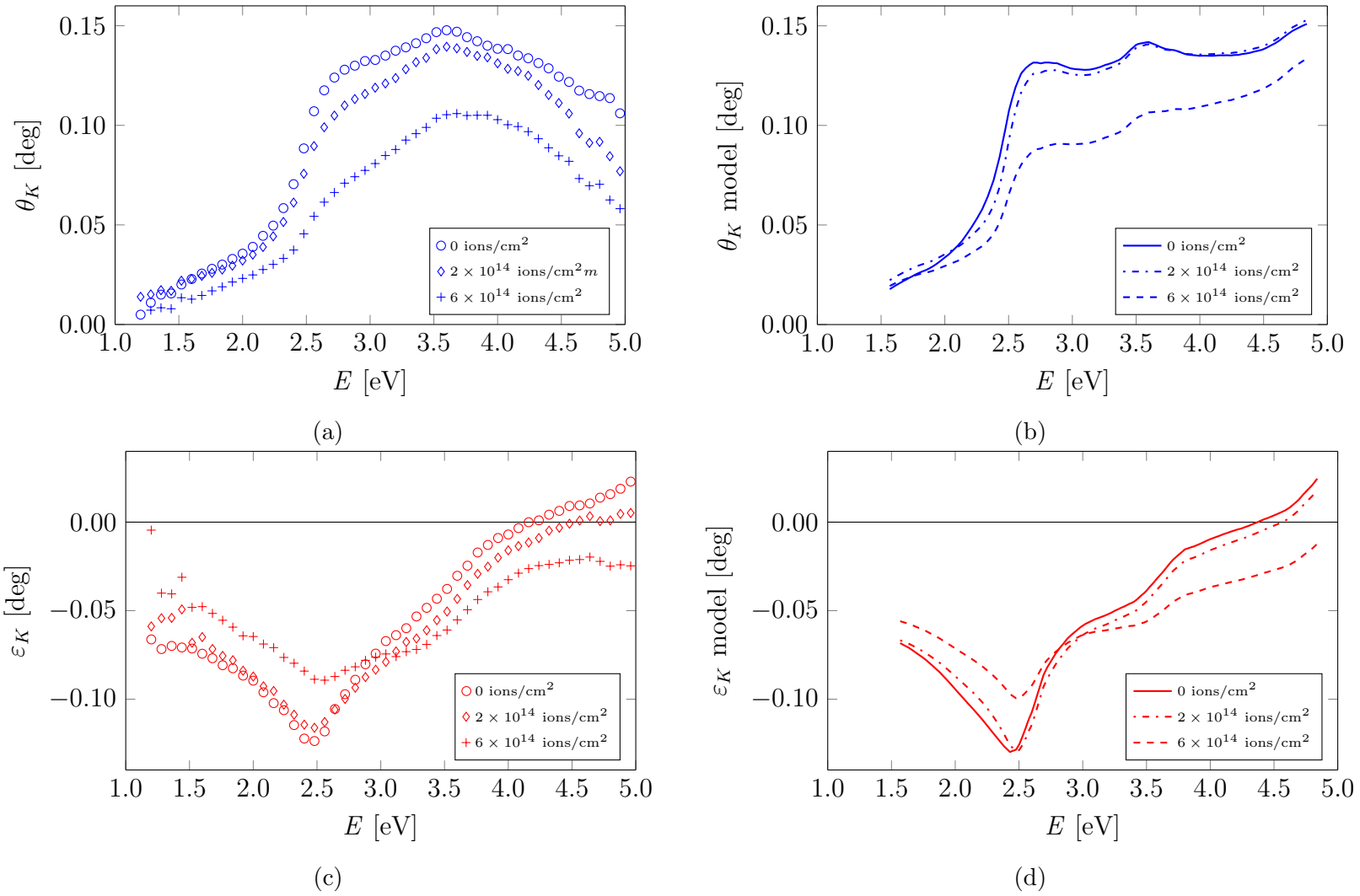

Figure 6.20: Polar Kerr rotation and ellipticity spectra of Al_2O_3(0001)/Pt (20 nm)/Au (20 nm)/Co (3 nm)/Au (5 nm) irradiated by various ion fluences and the theoretical models.

Table 6.5: Layer thicknesses for which the best agreement between the measured PMOKE spectra and the theoretical calculations was achieved for the Al_2O_3/Pt/Au/Co/Au sample set irradiated with ions.

	0 ions/cm^2	2×10^{14} ions/cm^2	6×10^{14} ions/cm^2
	Layer thickness [nm]	Layer thickness [nm]	Layer thickness [nm]
Au	5	1.4	0
EMA: 20 % Co, 80 % Au	0	2.8	0
EMA: 40 % Co, 60 % Au	0	2.2	0
EMA: 60 % Co, 40 % Au	0	0.1	0
EMA: 80 % Co, 20 % Au	0	0	0
Co	3	0	0
EMA: 80 % Co, 20 % Au	0	0	0
EMA: 60 % Co, 40 % Au	0	0.1	0
EMA: 40 % Co, 60 % Au	0	2.2	2.5
EMA: 20 % Co, 80 % Au	0	2.8	4.4
Au	20	16.4	15.58
Pt	20	20	20
Al_2O_3	-	-	-

The theoretical calculations describe the PMOKE spectra of the non-irradiated sample very well when nominal thicknesses are used as the parameters. The fact that the models fit well for this sample and did not for Al_2O_3/Pt/Co/Pt indicates that the properties of the Co layer vary based on the underlayer (the same constants of Co were used in both models).

The theoretical models feature modulations of the spectra around the photon energy 2.7 eV for Kerr rotation and 2.9 eV for Kerr ellipticity. These can be attributed to Au. The modulations are present in the measured spectra too but are much weaker indicating a difference between the actual optical constants of Au in the nanostructures and the constants taken from the literature.

It is worth mentioning that even though the comparison between the theoretical calculations and experiment indicate no intermixing for the as-grown structure it cannot be ruled out totally because the weak sensitivity of the spectra to this intermixing results in a high uncertainty of the determined layer thicknesses of intermixed Au and Co.

Irradiation with 2×10^{14} ions/cm^2 results in a slight decrease of amplitude of the PMOKE spectra. This is in accordance with the above-mentioned effect of intermixing of Co and Au. No pure Co is left in the nanostructure at this level of irradiation. Etching is negligent.

Further decrease of the PMOKE amplitude is visible after irradiation with the ion dose of 6×10^{14} ions/cm^2. The etching is high for this level of irradiation. The disagreement between the shape of the measured PMOKE spectra and the calculated ones might be caused by the approximations made in the calculations. The Co nanoparticles in Au were approximated by spheres but the shapes of the nanoparticles may vary in the sample. Also, the sample is approximated

as a number of layers with ideally flat interfaces but the interfaces in the real nanostructure are likely to be rough.

6.4 Modification of optical properties by voltage application

Unlike in the sections 6.2 and 6.3 induced changes of optical properties are investigated in this part. Previous work on samples containing Pt/Co/GdOx layers for which magnetic properties were modified by an electric field has shown that also other properties of the samples change. The samples in our current work contain no Co layer but the observed changes should be connected to the same mechanism as before - ion migration in an electric field.

The sample was attached to the translator stage of the ellipsometer and contacted by a BeCu probe tip. A picture of a contacted electrode taken by the camera of the ellipsometer is shown in figure 6.21.

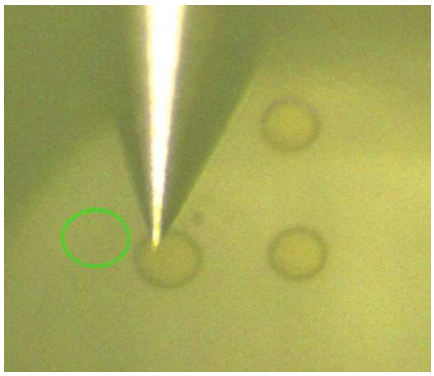

Figure 6.21: A picture of an electrode contacted by a BeCu probe tip before application of voltage. The green ellipse indicates the size of the light beam spot on the sample for the angle of incidence equal to 20 deg.

The measurements were done at a single angle of incidence which was 20 degrees. Such low incidence angle was chosen to achieve the smallest possible size of the spot. During measurements, the light also partly shined on the BeCu tip. Due to the shape and the position of the tip and because focusing probes were used we expect minimal effect on the results. Also, as the results presented here show only relative changes of optical properties the presence of the tip in the spot is not important.

A measurement of the ellipsometric parameters Ψ and Δ was carried out on a contacted electrode before applying the voltage to it. These parameters are plotted in figure 6.22.

+3 V were applied to the top Au electrode of the structure. *In situ* measurement mode of the ellipsometer was used to observe the time dependence of the changes of Ψ and Δ. Figure 6.23 shows the time evolution of Ψ for a few selected wavelengths.

No changes in Ψ are seen roughly for the first 14 minutes. Ψ then increases for the photon energy $E = 2.672$ eV which is close to the middle of the measured spectral region. The changes are then small for a few minutes before a

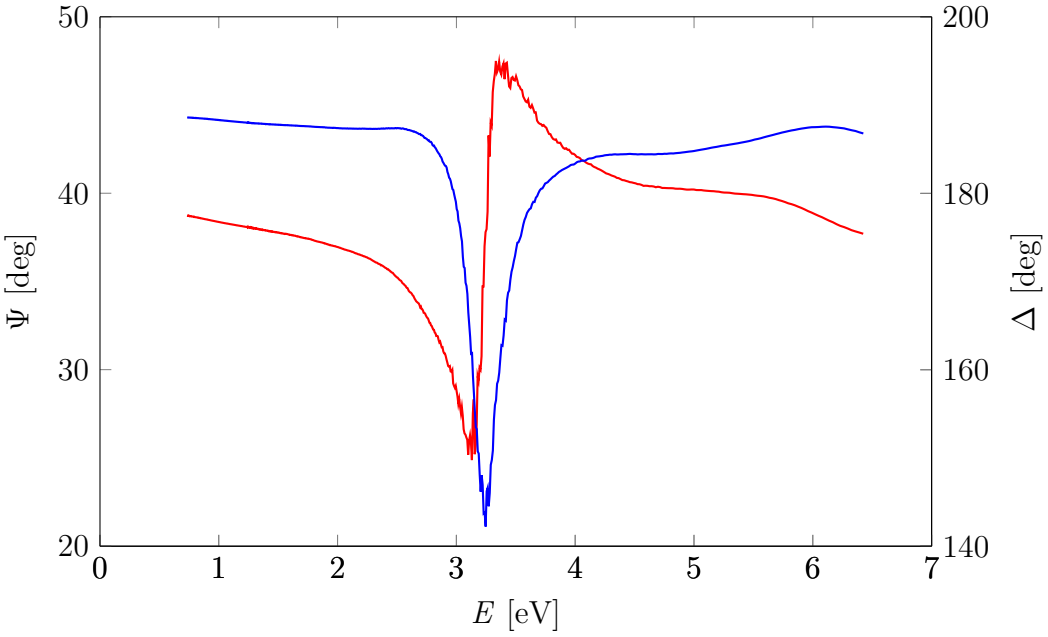

Figure 6.22: Parameters Ψ (blue line) and Δ (red line) measured on a contacted electrode before application of voltage.

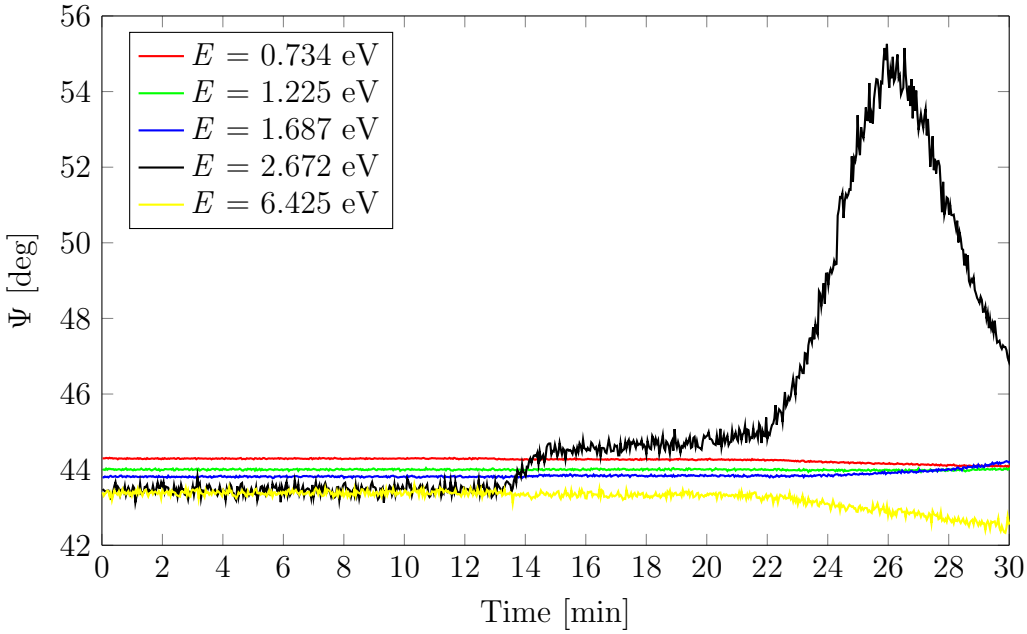

Figure 6.23: The time dependence of Ψ for a few photon energies upon application of +3 V to the top electrode.

modification of Ψ for all of the plotted energies is observed, especially strong for $E = 2.672$ eV.

Figure 6.24 shows the parameters Ψ and Δ after application of +3 V for 30 minutes. This measurement was carried out at zero voltage but the electrode was still contacted. The changes in the spectra are significant.

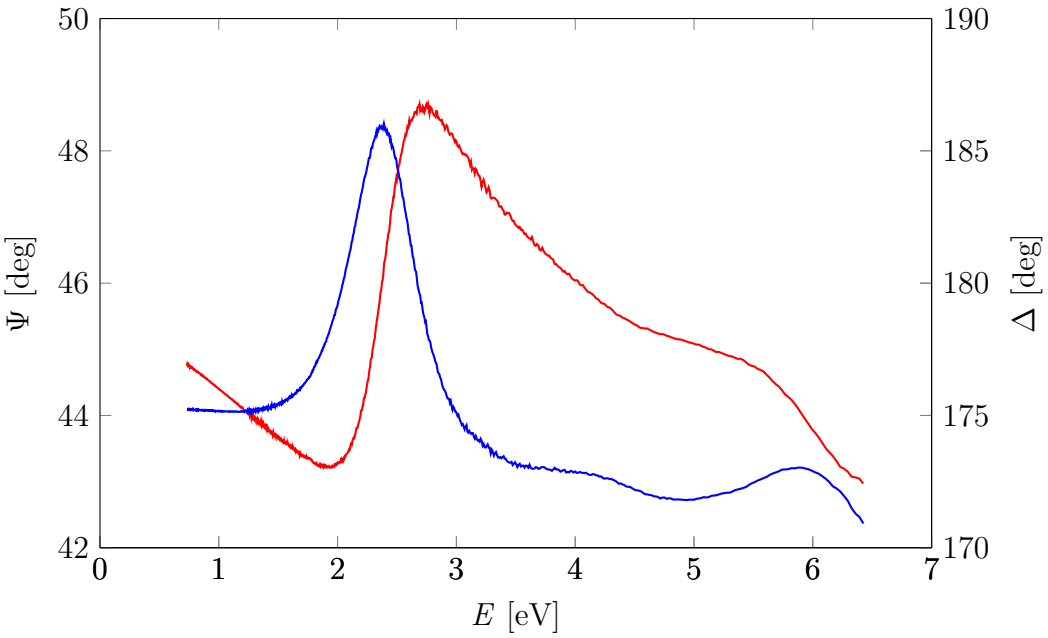

Figure 6.24: Parameters Ψ (blue line) and Δ (red line) measured on a contacted electrode after application of +3 V for 30 minutes.

The modification is also visible with naked eye, see figure 6.25.

We assume that the changes occur in the GdOx layer due to the migration of O^{2-} ions in the electric field. Also, there are indications from other experiments performed at MIT that the chemical properties of the top Au layer change with voltage too. That might affect the optical properties as well.

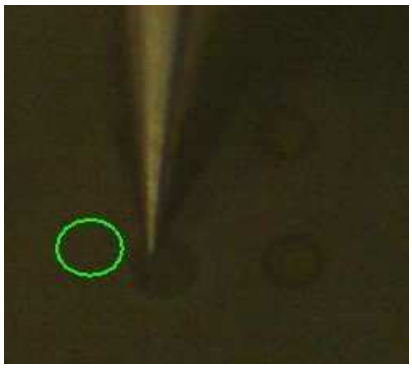

Figure 6.25: A picture of an electrode contacted by a BeCu probe tip after application of +3 V for 30 minutes.

In order to learn more about the process of the modification, the permittivity of the individual layers has to be fitted from the measured Ψ and Δ. However, that has proven complicated. A reason for this might be that the spot is slightly

bigger than the electrode. In that case, the areas around the electrode would contribute to the measured data and make fitting more difficult. Also, the probe tip might contribute to the experimental Ψ and Δ afterall. To rule out these possibilities and to enable measurements at higher angles of incidence we will receive a new set of samples with bigger top electrodes. Unfortunately, it is not possible to include the new set in this thesis.

Conclusion

Two methods of nonreversible modification of magnetic properties of ultrathin Co films sandwiched with either Pt or Au layers were investigated in this work - irradiation by a single pulse of soft X-rays and irradiation by 30 keV Ga^+ ions.

Polar Kerr rotation hysteresis loops measured on Pt/Co/Pt trilayers modified by soft X-rays revealed an enhancement of perpendicular magnetic anisotropy for certain irradiating energy densities. PMOKE spectra measured on the samples in the photon energy range from 1.2 eV to 5 eV are strongly modified for higher irradiating energy densities.

The experimental PMOKE spectra were compared to a theoretical calculation. Intermixing of the Co and Pt layers and evaporation of material upon irradiation was assumed in the models. The profile of the samples modified by various energy densities was determined from the best agreement between the experimental and calculated data. The models provide a reasonable agreement with the experiment. A presence of a CoPt alloy with 28 % is indicated by the comparison with theoretical calculations. This is close to the composition of the disordered $CoPt_3$ alloy with high magnetic anisotropy. The creation of the disordered $CoPt_3$ alloy upon irradiation might be the reason for the observed changes in magnetic properties.

Ion irradiation enhances the perpendicular magnetic anisotropy of Pt/Co/Pt trilayers for certain ion doses. On the other hand, the effects of the ion irradiation on the magnetic properties of Au/Co/Au are minimal.

Theoretical calculations describe the changes in PMOKE spectra of Pt/Co/Pt and Au/Co/Au with ion irradiation well and the profiles of the samples are determined.

The results of the theoretical calculations for the non-irradiated Pt/Co/Pt and Au/Co/Au samples suggest that the Co properties vary with the underlayer.

A modification of optical properties of a Ta/Pt/GdOx/Au device through voltage application was demonstrated. The fitting of the ellipsometric angles Ψ and Δ proved difficult. A modification in the device design is necessary to obtain better data for fitting.

Bibliography

[1] C. Chappert, A. Fert, and F. N. Van Dau. The emergence of spin electronics in data storage. *Nature Materials*, 6(11):813–823, November 2007.

[2] S. A. Wolf, D. D. Awschalom, R. A. Buhrman, J. M. Daughton, S. von Molnár, M. L. Roukes, A. Y. Chtchelkanova, and D. M. Treger. Spintronics: A spin-based electronics vision for the future. *Science*, 294(5546):1488–1495, November 2001.

[3] S. S. P. Parkin, M. Hayashi, and L. Thomas. Magnetic domain-wall racetrack memory. *Science*, 320(5873):190–194, April 2008.

[4] M. Mitchell Waldrop. The chips are down for Moore's law. *Nature*, 530(7589):144–147, February 2016.

[5] D. A. Allwood, G. Xiong, C. C. Faulkner, D. Atkinson, D. Petit, and R. P. Cowburn. Magnetic domain-wall logic. *Science*, 309(5741):1688–1692, September 2005.

[6] J. M. D. Coey. *Magnetism and Magnetic Materials*. Cambridge University Press, 2010.

[7] W. J. M. de Jonge, P. J. H. Bloemen, and F. J. A. den Broeder. *Ultrathin Magnetic Structures I*, chapter Experimental investigations of magnetic anisotropy. Springer, 2005.

[8] G.A. Bertero and R. Sinclair. Structure-property correlations in Pt/Co multilayers for magneto-optic recording. *Journal of Magnetism and Magnetic Materials*, 134(1):173–184, May 1994.

[9] G. A. Bertero, R. Sinclair, C.-H. Park, and Z. X. Shen. Interface structure and perpendicular magnetic anisotropy in Pt/Co multilayers. *Journal of Applied Physics*, 77(8):3953–3959, April 1995.

[10] P. F. Carcia, S. I. Shah, and W. B. Zeper. Effect of energetic bombardment on the magnetic coercivity of sputtered Pt/Co thin-film multilayers. *Applied Physics Letters*, 56(23):2345–2347, June 1990.

[11] L. Néel. Magnetic surface anisotropy and superlattice formation by orientation. *Journal de Physique et le Radium*, 15(4):225–239, April 1954.

[12] G. Schütz, S. Stähler, M. Knülle, P. Fischer, S. Parkin, and H. Ebert. Distribution of magnetic moments in Co/Pt and Co/Pt/Ir/Pt multilayers detected by magnetic x-ray absorption. *Journal of Applied Physics*, 73(10):6430–6432, May 1993.

[13] B. Zhang, Kannan M. Krishnan, C. H. Lee, and R. F. C. Farrow. Magnetic anisotropy and lattice strain in Co/Pt multilayers. *Journal of Applied Physics*, 73(10):6198–6200, May 1993.

[14] R. M. Bozorth. Magnetostriction and crystal anisotropy of single crystals of hexagonal cobalt. *Physical Review*, 96(2):311–316, October 1954.

[15] B. N. Engel, M. H. Wiedmann, and C. M. Falco. Overlayer-induced perpendicular anisotropy in ultrathin Co films (invited). *Journal of Applied Physics*, 75(10):6401–6405, May 1994.

[16] M. Kisielewski, A. Maziewski, M. Tekielak, A. Wawro, and L. T. Baczewski. New possibilities for tuning ultrathin cobalt film magnetic properties by a noble metal overlayer. *Physical Review Letters*, 89(8), August 2002.

[17] C. Chappert, H. Bernas, J. Ferré, V. Kottler, J.-P. Jamet, Y. Chen, E. Cambril, T. Devolder, F. Rousseaux, V. Mathet, and H. Launois. Planar patterned magnetic media obtained by ion irradiation. *Science*, 280(5371):1919–1922, June 1998.

[18] C. Vieu, J. Gierak, H. Launois, T. Aign, P. Meyer, J. P. Jamet, J. Ferré, C. Chappert, T. Devolder, V. Mathet, and H. Bernas. Modifications of magnetic properties of Pt/Co/Pt thin layers by focused gallium ion beam irradiation. *Journal of Applied Physics*, 91(5):3103–3110, March 2002.

[19] A. Maziewski, P. Mazalski, Z. Kurant, M. O. Liedke, J. McCord, J. Fassbender, J. Ferré, A. Mougin, A. Wawro, L. T. Baczewski, A. Rogalev, F. Wilhelm, and T. Gemming. Tailoring of magnetism in Pt/Co/Pt ultrathin films by ion irradiation. *Physical Review B*, 85(5), February 2012.

[20] T. Shima and K. Takanashi. *Handbook of Magnetism and Advanced Magnetic Materials*, chapter Hard Magnetic Films. John Wiley & Sons Inc, 2007.

[21] M. Sakamaki, K. Amemiya, M. O. Liedke, J. Fassbender, P. Mazalski, I. Sveklo, and A. Maziewski. Perpendicular magnetic anisotropy in a Pt/Co/Pt ultrathin film arising from a lattice distortion induced by ion irradiation. *Physical Review B*, 86(2), July 2012.

[22] P. Mazalski, Z. Kurant, A. Maziewski, M. O. Liedke, J. Fassbender, L. T. Baczewski, and A. Wawro. Ion irradiation induced enhancement of out-of-plane magnetic anisotropy in ultrathin Co films. *Journal of Applied Physics*, 113(17):17C109, May 2013.

[23] C. T. Rettner, S. Anders, J. E. E. Baglin, T. Thomson, and B. D. Terris. Characterization of the magnetic modification of Co/Pt multilayer films by He^+, Ar^+, and Ga^+ ion irradiation. *Applied Physics Letters*, 80(2):279–281, January 2002.

[24] J. Fassbender, M. O. Liedke, T. Strache, W. Möller, E. Menéndez, J. Sort, K. V. Rao, S. C. Deevi, and J. Nogués. Ion mass dependence of irradiation-induced local creation of ferromagnetism in $Fe_{60}Al_{40}$ alloys. *Physical Review B*, 77(17), May 2008.

[25] K. A. Avchaciov, W. Ren, F. Djurabekova, K. Nordlund, I. Sveklo, and A. Maziewski. Modification of Pt/Co/Pt film properties by ion irradiation. *Physical Review B*, 92(10):104109, September 2015.

[26] C. Chappert and P. Bruno. Magnetic anisotropy in metallic ultrathin films and related experiments on cobalt films (invited). *Journal of Applied Physics*, 64(10):5736–5741, November 1988.

[27] P. Mazalski, I. Sveklo, Z. Kurant, K. Ollefs, A. Rogalev, F. Wilhelm, J. Fassbender, L. T. Baczewski, A. Wawro, and A. Maziewski. XAS and XMCD studies of magnetic properties modifications of Pt/Co/Au and Pt/Co/Pt trilayers induced by Ga^+ ions irradiation. *Journal of Synchrotron Radiation*, 22(3):753–759, April 2015.

[28] W. Möller, W. Eckstein, and J. P. Biersack. Tridyn-binary collision simulation of atomic collisions and dynamic composition changes in solids. *Computer Physics Communications*, 51(3):355–368, November 1988.

[29] K.H.J. Buschow, P.G. van Engen, and R. Jongebreur. Magneto-optical properties of metallic ferromagnetic materials. *Journal of Magnetism and Magnetic Materials*, 38(1):1–22, August 1983.

[30] E. Lišková, M. Veis, Š. Višňovský, J. Ferré, A. Mougin, P. Mazalski, A. Maziewski, M.O. Liedke, and J. Fassbender. Effect of Ga^+ irradiation on the magneto-optic spectra of Pt/Co/Pt sandwiches. *Thin Solid Films*, 520(24):7169–7172, October 2012.

[31] E. Jakubisova-Liskova, S. Visnovsky, A. Wawro, L. T. Baczewski, P. Mazalski, A. Maziewski, M. O. Liedke, J. McCord, and J. Fassbender. Effect of Ga^+ irradiation in molecular-beam epitaxy grown Pt/Co/Pt thin films studied by magneto-optic spectroscopy. *Journal of Applied Physics*, 115(17):17C106, May 2014.

[32] M. Galeotti, A. Atrei, U. Bardi, B. Cortigiani, G. Rovida, and M. Torrini. Epitaxy and alloying at the Co/Pt(111) interface: a study by X-ray photoelectron diffraction. *Surface Science*, 297(2):202–208, November 1993.

[33] F. J. A. den Broeder, D. Kuiper, A. P. van de Mosselaer, and W. Hoving. Perpendicular magnetic anisotropy of Co-Au multilayers induced by interface sharpening. *Physical Review Letters*, 60(26):2769–2772, June 1988.

[34] N. I. Polushkin, V. Oliveira, O. Conde, R. Vilar, Yu. N. Drozdov, A. Apolinário, A. García-García, J. M. Teixeira, and G. N. Kakazei. Evidences for direct magnetic patterning via diffusive transformations using femtosecond laser interferometry. *Applied Physics Letters*, 101(13):132408, September 2012.

[35] A. Aktag, S. Michalski, L. Yue, R. D. Kirby, and S.-H. Liou. Formation of an anisotropy lattice in Co/Pt multilayers by direct laser interference patterning. *Journal of Applied Physics*, 99(9):093901, May 2006.

[36] C. Schuppler, A. Habenicht, I. L. Guhr, M. Maret, P. Leiderer, J. Boneberg, and M. Albrecht. Control of magnetic anisotropy and magnetic patterning of perpendicular Co/Pt multilayers by laser irradiation. *Applied Physics Letters*, 88(1):012506, January 2006.

[37] J. Kisielewski, K. Postava, I. Sveklo, A. Nedzved, P. Trzciński, A. Maziewski, B. Szymański, M. Urbaniak, and F. Stobiecki. Magnetic anisotropy of Co films annealed by laser pulses. *Solid State Phenomena*, 140:69–74, 2008.

[38] J. Kisielewski, W. Dobrogowski, Z. Kurant, A. Stupakiewicz, M. Tekielak, A. Kirilyuk, A. Kimel, Th. Rasing, L. T. Baczewski, A. Wawro, K. Balin, J. Szade, and A. Maziewski. Irreversible modification of magnetic properties of Pt/Co/Pt ultrathin films by femtosecond laser pulses. *Journal of Applied Physics*, 115(5):053906, February 2014.

[39] I. Sveklo, Z. Kurant, A. Bartnik, D. Klinger, R. Sobierajski, A. Wawro, J. Kisielewski, M. Tekielak, and A. Maziewski. Modification of magnetic properties of Pt/Co/Pt trilayers driven by nanosecond pulses of extreme ultraviolet irradiation. *Journal of Physics D: Applied Physics*, 50(2):025001, November 2016.

[40] E. Dynowska, J. B. Pelka, D. Klinger, R. Minikayev, A. Bartnik, P. Dluzewski, M. Jakubowski, M. Klepka, A. Petruczik, O. H. Seeck, R. Sobierajski, I. Sveklo, A. A. Wawro, and A. Maziewski. Structural investigation of ultrathin Pt/Co/Pt trilayer films under EUV irradiation. *Nuclear Instruments and Methods in Physics Research Section B: Beam Interactions with Materials and Atoms*, 364:33–39, August 2015. 12th International School and Symposium on Synchrotron Radiation in Natural Science.

[41] J. O. Cross, M. Newville, B. B. Maranville, C. Bordel, F. Hellman, and V. G. Harris. Evidence for nanoscale two-dimensional Co clusters in $CoPt_3$ films with perpendicular magnetic anisotropy. *Journal of Physics: Condensed Matter*, 22(14):146002, March 2010.

[42] A.J. Schellekens, A. van den Brink, J.H. Franken, H.J.M. Swagten, and B. Koopmans. Electric-field control of domain wall motion in perpendicularly magnetized materials. *Nature Communications*, 3:847, May 2012.

[43] U. Bauer, S. Emori, and G. S. D. Beach. Voltage-controlled domain wall traps in ferromagnetic nanowires. *Nature Nanotechnology*, 8(6):411–416, May 2013.

[44] N. Lei, T. Devolder, G. Agnus, P. Aubert, L. Daniel, J.-V. Kim, W. Zhao, T. Trypiniotis, R. P. Cowburn, C. Chappert, D. Ravelosona, and P. Lecoeur. Strain-controlled magnetic domain wall propagation in hybrid piezoelectric/ferromagnetic structures. *Nature Communications*, 4:1378, January 2013.

[45] M. K. Niranjan, C.-G. Duan, S. S. Jaswal, and E. Y. Tsymbal. Electric field effect on magnetization at the Fe/MgO(001) interface. *Applied Physics Letters*, 96(22):222504, May 2010.

[46] U. Bauer, S. Emori, and G. S. D. Beach. Voltage-gated modulation of domain wall creep dynamics in an ultrathin metallic ferromagnet. *Applied Physics Letters*, 101(17):172403, October 2012.

[47] A. Manchon, C. Ducruet, L. Lombard, S. Auffret, B. Rodmacq, B. Dieny, S. Pizzini, J. Vogel, V. Uhlíř, M. Hochstrasser, and G. Panaccione. Analysis of oxygen induced anisotropy crossover in Pt/Co/MOx trilayers. *Journal of Applied Physics*, 104(4):043914, August 2008.

[48] J. J. Yang, F. Miao, M. D. Pickett, D. A. A. Ohlberg, D. R. Stewart, C. N. Lau, and R. S. Williams. The mechanism of electroforming of metal oxide memristive switches. *Nanotechnology*, 20(21):215201, May 2009.

[49] U. Bauer, L. Yao, A. J. Tan, P. Agrawal, S. Emori, H. L. Tuller, S. van Dijken, and G. S. D. Beach. Magneto-ionic control of interfacial magnetism. *Nature Materials*, 14(2):174–181, November 2014.

[50] L. Ohnoutek. Study of dynamically induced changes of magnetic properties in nanostructures. Bachelor's thesis, Faculty of Mathematics and Physics, Charles University, Prague, Czech Republic, 2015. Language: Czech.

[51] M. Nývlt. *Optical interactions in ultrathin magnetic film structures.* Doctoral thesis, Faculty of Mathematics and Physics, Charles University, Prague, Czech Republic, 1996.

[52] P. S. Pershan. Magneto-optical effects. *Journal of Applied Physics*, 38(3):1482–1490, 1967.

[53] Š Višňovský. Magneto-optical ellipsometry. *Czechoslovak Journal of Physics B*, 36(5):625–650, May 1986.

[54] P. Yeh. Optics of anisotropic layered media: A new 4×4 matrix algebra. *Surface Science*, 96(1):41–53, 1980.

[55] J. Peatross and M. Ware. *Physics of Light and Optics.* Available at `optics.byu.edu`, 2015 edition.

[56] J. A. Woollam Co. Ellipsometry tutorial. Available at `www.jawoollam.com/resources/ellipsometry-tutorial`.

[57] K. Jungwirth, A. Cejnarova, L. Juha, B. Kralikova, J. Krasa, E. Krousky, P. Krupickova, L. Laska, K. Masek, T. Mocek, M. Pfeifer, A. Präg, O. Renner, K. Rohlena, B. Rus, J. Skala, P. Straka, and J. Ullschmied. The Prague Asterix Laser System. *Physics of Plasmas*, 8(5):2495–2501, April 2001.

[58] A. Bartnik, H. Fiedorowicz, R. Jarocki, J. Kostecki, M. Szczurek, and P.W. Wachulak. Laser-plasma EUV source dedicated for surface processing of polymers. *Nuclear Instruments and Methods in Physics Research Section A: Accelerators, Spectrometers, Detectors and Associated Equipment*, 647(1):125–131, August 2011.

[59] B. Johs and J. S. Hale. Dielectric function representation by B-splines. *physica status solidi (a)*, 205(4):715–719, 2008.

[60] D. W. Lynch and W. R. Hunter. *Handbook of Optical Constants of Solids, Vol. 2.* Academic Press, 1998.

[61] H. Brandle, D. Weller, J. C. Scott, S. S. P. Parking, and C.-J. Lin. Optical and magneto-optical characterization of evaporated Co/Pt alloys and multilayers. *IEEE Transactions on Magnetics*, 28(5):2967–2969, September 1992.

[62] S. Visnovsky, M. Nyvlt, V. Parizek, P. Kielar, V. Prosser, and R. Krishnan. Magneto-optical studies of Pt/Co multilayers and Pt-Co alloy thin films. *IEEE Transactions on Magnetics*, 29(6):3390–3392, November 1993.

[63] M. Abe and M. Gomi. Magneto-optical effect and effective dielectric tensor in composite material containing magnetic fine particles or thin layers. *Japanese Journal of Applied Physics*, 23(12R):1580, 1984.

List of Abbreviations

AFM	Atomic force microscopy
EDXA	Energy dispersive X-ray analysis
EMA	Effective medium approximation
EUV	Extreme ultraviolet
EXAFS	Extended X-ray absorption fine structure
HDD	Hard disk drive
HRTEM	High-resolution transmission electron microscopy
LMOKE	Longitudinal magneto-optical Kerr effect
MBE	Molecular beam epitaxy
MRAM	Magnetic random access memory
PMA	Perpendicular magnetic anisotropy
PMOKE	Polar magneto-optical Kerr effect
PMOKR	Polar magneto-optical Kerr rotation
RAM	Random access memory
TEM	Transmission electron microscopy
TMOKE	Transversal magneto-optical Kerr effect
ToF-SIMS	Time of flight secondary ion mass spectroscopy
XMCD	X-ray magnetic circular dichroism
XRR	X-ray reflectivity